THE UNIVERSITY OF HULL

The Limitations of Rankine-Hugoniot Jump Conditions for Estimating Infall Velocity during a Minor Galaxy Cluster Merger

being a Thesis submitted for the Degree of Master of Science by Research

in the University of Hull

by

Matilda Lena-Robert Huntley, BSc (Hons)

April 2023

"Therefore I think and judge it for thy best

Thou follow me, and I will be thy guide,

And lead thee hence through the eternal place,"

– Dante Alighieri, *Divine Comedy,*

Cantica I: Inferno, Canto I, Stanza XXXVIII

Acknowledgements

I wish to thank Dr. Elke Roediger for her tutelage, expertise, understanding, patience, and her kindness. This thesis would not have been possible without her support.

Thanks are also in order to Professor Brad Gibson, and the wonderful department that I am so grateful to have been part of. Thank you to the galaxy cluster group, and Iraj Vaezzadeh for coaching me so well on using HPC and Python. A big thank you to the VIPER team as well.

Beyond astrophysics, to my friends and family, old and new, many thanks. Bridge, thank you so much. My parents, thank you for always believing in me. Finally, I pay special thanks to my grandparents: Nadine and Peter. For supporting and encouraging me, always, thank you.

Declaration of Originality

This thesis is submitted in partial fulfilment of the degree of Master of Science from the University of Hull. I declare that the work undertaken in this thesis is original and my own and was carried out under the supervision of Dr. Elke Roediger and Prof. Brad Gibson from the University of Hull.

The work that has been, or will be, published from this thesis was my principle responsibility. Notably driving the science project, analysis, and writing up. Where work, results, or ideas have been taken from other sources, those sources are explicitly referenced.

Candidates signature: 

Date: 2023 / 04 / 05

Abstract

Galaxy cluster mergers occur frequently in the universe. As a merging cluster, or subcluster, falls into the gravity well of the host cluster, their intra-cluster mediums (ICMs) interact. The supersonic motion of the infaller leads to the formation of a bow shock, ahead of the infaller. In ideal conditions, the shock speed can be derived from the contrast in density and temperature across the shock via Rankine-Hugoniot jump conditions (RHJCs). In this thesis, we determine to what extent RHJCs can be used to measure the infaller's speed. The infall velocity is a useful quantity to the astrophysical community. It can be used to explore the dynamical history of galaxy clusters, unlocking insight into large-scale cosmic structures. This thesis considers a 1:10 minor merger, simulated using the hydrodynamic and N-body code FLASH. Using RHJCs, we estimate infall velocity of the merging subcluster throughout the evolution of our simulated merger. We also measure the velocity for the DM and gas halos directly from the simulation data, comparing RH velocity estimates against simulation velocities. We find that, during the infall phase, RH based infaller speed estimates are within $15-35\%$ to the infall velocity until $\sim 100-200$ Myr after pericenter passage. We note a tendency to underestimate infaller speed, and that disturbance in the ICM can further contribute to this underestimation bias. Beyond pericenter passage, RH velocity estimates quickly become unrelated to the infall velocity of the subcluster. As the infalling subcluster is no longer driving the bow shock, here RHJCs will always overestimate infaller velocity.

Contents

List of Figures

List of Tables

1. Introduction

1.1 Galaxy Clusters and the Intracluster Medium

Within our universe, galaxy clusters are some of the largest known structures. Much larger than individual or groups of galaxies, these systems of galaxies no longer separate as the universe expands. Instead, they are bound together by the attractive force of gravity. Member galaxies, numbering in the hundreds or thousands, are bound by a common gravitational potential (Sparke & Gallagher, 2007).

Galaxy clusters are made up of their component galaxies, the enveloping intracluster medium (ICM), and dark matter (DM). Cluster masses range from several 10^{13} to 10^{15} $M_{\odot}$ (Pratt et al., 2019). For a given galaxy cluster, DM makes up 80% of the mass and the ICM contributes about 15% (Schneider, 2006). The existence of DM has been argued based on its effects, e.g. the high virial velocity and ICM virial temperature of cluster galaxies, gravitational lensing, the evidence for which points towards prevalence of DM (e.g. Girardi et al., 1996; Markevitch & Vikhlinin, 2007; Kravtsov & Borgani, 2012; Wechsler & Tinker, 2018). The currently accepted model, known as ΛCDM, incorporates current understandings of DM, and dark energy, alongside baryonic matter to describe the universe.

The atmosphere that fills a galaxy cluster is known as the ICM. A fully ionised plasma, composed of primordial hydrogen, helium, alongside trace metals, the ICM reaches temperatures of $10^7 - 10^8$K (Mitchell et al., 1976; Mernier et al., 2018). As consequence, the component gases split into proton, ion, and electron fluids. Gravity is the force responsible for heating and binding the ICM (Sparke & Gallagher, 2007). The ICM itself emits X-rays, and unlike the point sources of active galactic nuclei (AGN), the X-ray emission of galaxy cluster's ICM is diffuse (Markevitch & Vikhlinin, 2007). As seen in figure 1.1, centered here on the brightest cluster galaxy (BCG), NGC 1275, the Perseus cluster is host to thousands of member galaxies and is thought to span well over a Mpc in diameter (Simionescu et al., 2011).

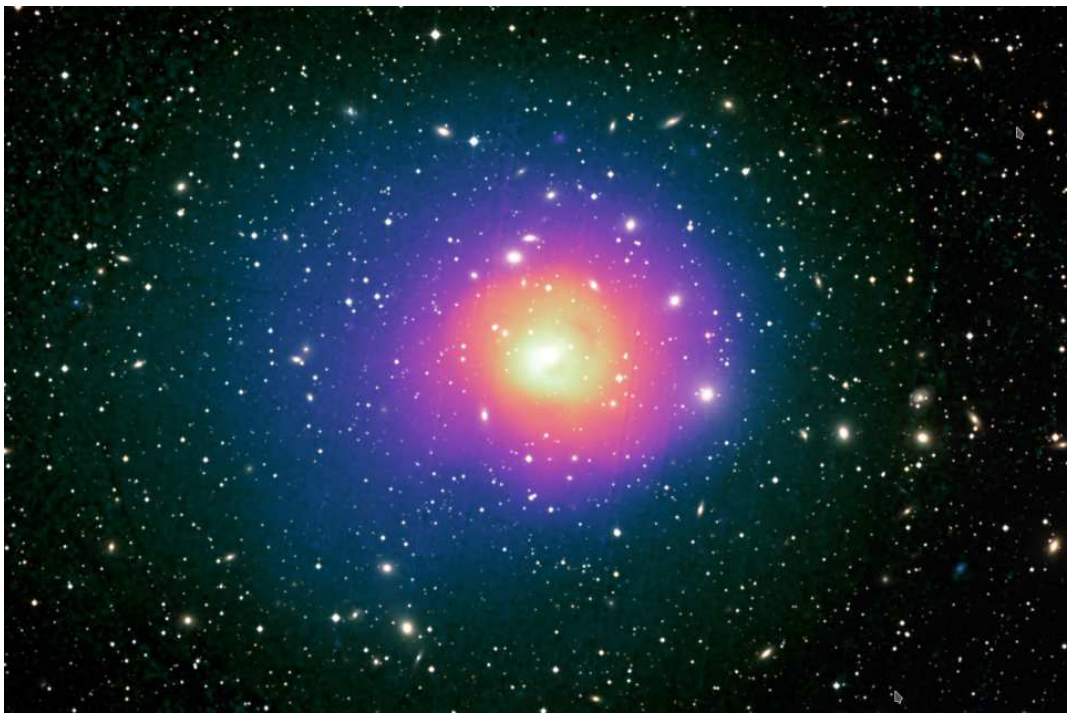

Figure 1.1: A composite Hubble / XMM-Newton image, showing Perseus observed in both optical and X-ray light (ESA et al., 2020). Here, X-ray surface brightness is represented as colour, scaling from blue (lowest) to white (highest).

The X-ray 'shroud' encapsulating the central galaxies in the image is Perseus' ICM. As the ICM is a plasma, it emits X-ray light via thermal bremsstrahlung (Gould, 1980). Temperature corresponds to the mean kinetic energy of particles and as such the photons emitted from the ICM, due to its high temperatures, are X-rays. X-ray images reveal the structure of the ICM. Generally, the ICM has a declining radial density profile. Modern X-ray images also reveal shocks and cold fronts (e.g. Keshet et al., 2010; review by Markevitch & Vikhlinin, 2007). X-ray spectroscopy allows us to directly determine the temperature, pressure, and density of the ICM surrounding the cluster.

Over human timescales, galaxy clusters can appear as static and unchanging entities. However, thanks insights garnered from X-ray observations and continuing research we understand that they evolve independent of mergers as well. We have mentioned already their makeup of component galaxies, DM, and ICM as well as the X-ray 'hot' nature of this encompassing ICM. Galaxy clusters relax and cool, undergoing a process known as 'virialization' where they become stable. In turn, they can be reheated by AGN feedback, even a cluster

that appears 'relaxed' and stable can be turbulent and changing beneath the surface (e.g. Markevitch & Vikhlinin, 2007; Forman et al., 2007).

1.2 Galaxy Cluster Mergers

Mergers between galaxy clusters are violent and energetic. They are also fairly common; Perseus, as mentioned above, hosts thousands of member galaxies and is likely the combined product of countless individual merger events (Roukema et al., 1993; Kravtsov & Borgani, 2012). Perseus is one of many observed merging galaxy clusters, other examples include, but are not limited to, the 'Bullet' cluster (Tucker et al., 1998; Markevitch et al., 2002), Virgo (Irwin & Sarazin, 1996), A520 (Markevitch et al., 2005), and Coma (Neumann et al., 2001). Gravity traps the merging galaxy clusters within their combined spheres of influence, eventually, over the course of Gyrs, they draw close enough for their atmospheres to interact. The 'infalling' cluster, or subcluster, descends through the gravitational potential well of the 'host cluster', reaching relative speeds of thousands of kilometers per second. The infaller moves through the host's potential well in one or more 'passages', ending with the eventual merging of the infaller into the host. The angle at which the infaller approaches the host cluster, part of the impact parameters, is important, and ranges from direct 'head-on' collisions to much more shallow, glancing approaches. This, amongst other factors, effects the number of infall periods a given merger event might have. The first time an infalling subcluster travels towards the host cluster's center is known as 'first infall'. Pericenter is the position where the distance between both cluster centers, is smallest. The opposite, apocenter and apocenter passage, is true when the infaller is furthest away from that of the host cluster before falling back into its potential well. This process, from start to finish, can take a few billion years and forms a combined, and consequently more massive, galaxy cluster (Sparke & Gallagher, 2007; Zhang et al., 2016).

In a galaxy cluster merger, the infaller loses momentum and energy over time. The primary braking force acting on the infalling cluster is dynamical friction, with the main mechanism being gravity. As the infaller traverses the host cluster, it attracts matter which leads to an enhanced density in the infaller's wake. This overdensity accelerates matter

grouping further, with the combined gravity of this matter pulling back on the merging infaller. Post-pericenter passage an infalling subcluster decelerates until it reaches apocenter, beginning another infall period, or merging with the host altogether (e.g. White, 1976; Ostriker, 1999).

A 'major merger' is the merging of two clusters considered to have similar mass, a $\sim 1:1$ mass ratio. The masses involved drive effects to their extremes, resulting in violent mergers where the clusters can, quite literally, tear each other apart. Whilst observations of such events are spectacular, we are interested in the calmer, somewhat gentler, variation of galaxy cluster mergers.

1.3 Minor Mergers

Minor mergers differ from major mergers in that they involve a higher ratio of masses. Accepted ranges vary, but typically a mass ratio of $\sim 1:3$, or higher, between host and infaller would constitute a minor merger. These mergers are still energetic, but not as violent as major mergers. In this section, we discuss some of the general features of minor mergers and describe some pertinent examples.

For typical features in the ICM of a minor merger, we can expect the infaller's atmosphere to be truncated by the host's ICM and for the subcluster to develop a tail. In general, supersonic infall leads to the formation of a bow shock, the consequence of supersonic motion through the medium. We discuss gas shocks, and the pertinent anatomy of bow shocks, in more detail below in chapter 2 (See: figure 2.2). Where the infaller has already passed pericenter, the shock might have detached or runaway altogether. The motion of, and eventual merger, the infaller transfers angular momentum to the host cluster's ICM, creating a sloshing cold front around the host's core that can persist for some time (Ascasibar & Markevitch, 2006; Roediger et al., 2012; ZuHone & Roediger, 2016; Vaezzadeh et al., 2022). Figure 1.2 shows sloshing cold fronts in the Perseus cluster. Similar to the prior XMM-Newton observation, here Chandra and the work of Zhuravleva et al. (2014) shows us, instead, the structure of the Perseus ICM. The bottom image (b), featuring a residual image, allows us to see where relative ICM overdensities are. We can see an arc-shaped and spiral-shaped overdensity in

the ICM, with the gas in these areas disturbed from equilibrium, perturbed by what appears to be a late stage minor merger.

In a minor merger, as the infalling subcluster traverses the host's potential well, the ICMs of the merging clusters interact. The infaller moves through the host's ICM, which exerts a pressure on the infaller's atmosphere. We know this as 'ram pressure'. As the infaller moves towards the host's core, the infaller's atmosphere is compressed at the upstream edge. This pressure sweeps the atmosphere of the infaller backwards, stripping away the gas of the infaller over time. As ram pressure strength is proportional to the density and infall velocity squared, this effect becomes pronounced at pericenter passage. The pressure can become so intense that the merging cluster's gaseous core can be uprooted from the bottom of it's own gravitational well, as the DM halo is not subject to ram pressure, decoupling the DM and gas halos from one another. The 'Bullet cluster', or 1E 0657-56, is an example of such extreme stripping. Featuring a host mass of $\sim 10^{15}$ $M_{\odot}$ and an infaller mass of $\sim 10^{14}$ $M_{\odot}$, the Bullet cluster fits the definition for a minor merger. Observable 'nearly exactly in the plane of the sky' (Springel & Farrar, 2007, see also: Barrena et al., 2002; Markevitch et al., 2002), the infalling subcluster or 'bullet', has passed almost directly through the center of the host cluster. This can be seen in figure 1.3, comparing a simulated model to reality in X-ray. Both the real-life and simulated merger feature roughly the same scale and colour range. The famous 'bullet' of the Bullet cluster can be seen as a sort of blunt wedge, directly east of the main clusters central white mass. A prominent bow shock has formed directly ahead of the infallers gas halo, caused by the blunt shape of the infaller and supersonic motion relative to the traversed medium (Markevitch et al., 2002). Seen as the change in surface brightness from red to green ahead of the bullet, where there is a thin boundary, or contact discontinuity, between higher and lower intensity x-ray brightness. In their work, Springel & Farrar (2007) demonstrated the inferred shock velocity of the bullet is not necessarily the speed of the infaller's gas or DM halos, and that the subcluster's velocity is lower than the speed of the shock itself. Using N-body and smoothed particle hydrodynamical simulations to investigate the dynamic history of the merging galaxy cluster, the simulation basis was derived from a 500 ks Chandra X-ray observation. This enabled the authors to closely match the simulated model clusters to the

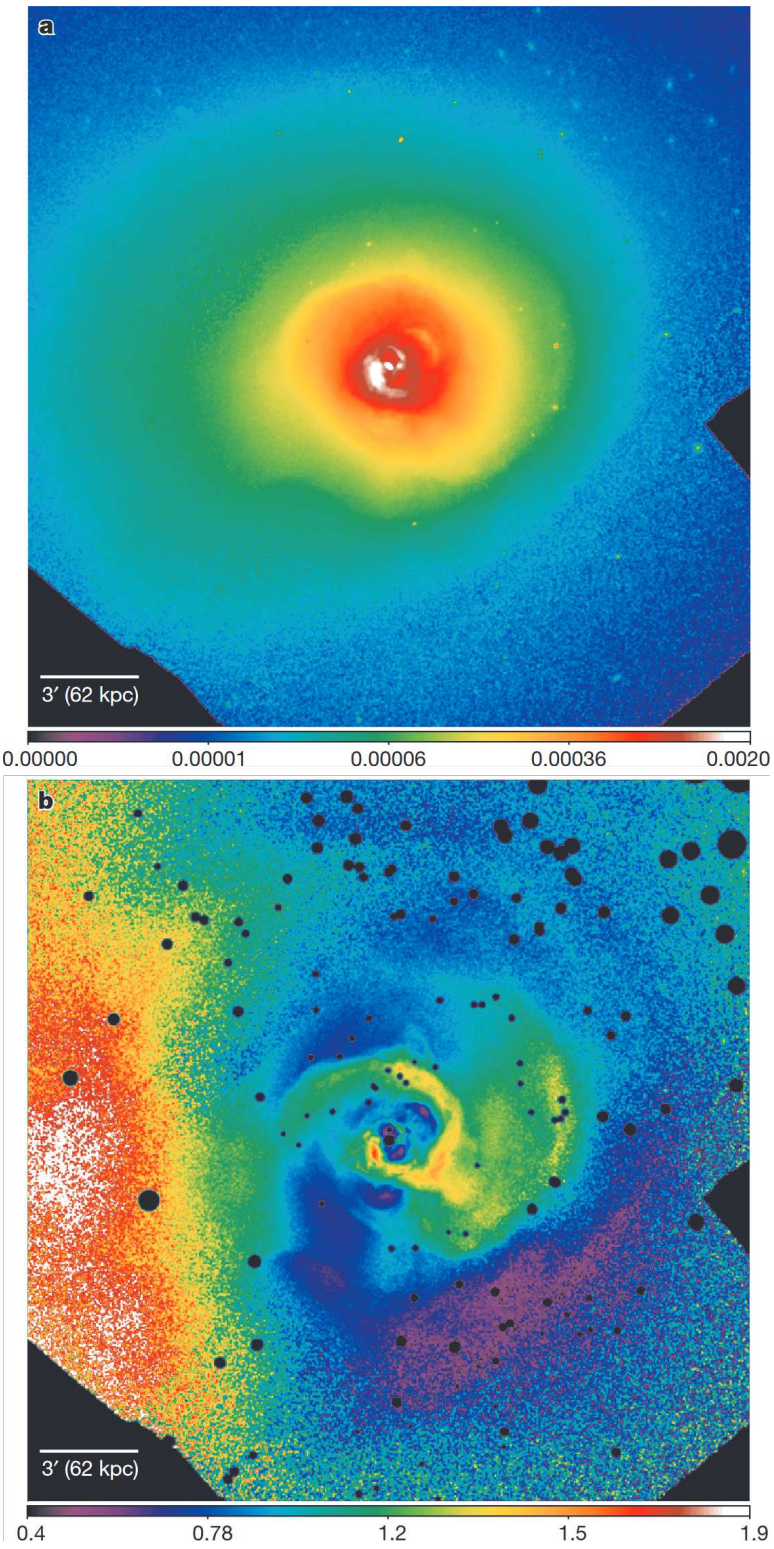

Figure 1.2: X-ray images of the Perseus galaxy cluster, taken from Chandra observations in the energy range of 0.5 – 3.5 keV (Figure 1a & 1b; Zhuravleva et al., 2014). **a:** Mosaic image of X-ray surface brightness in counts per second per pixel. **b:** Residual image made by dividing mosaic by a symmetric spherical β-model (see: section 3.1.1). The black dots correspond to removed point sources, i.e. emissions from sources other than the ICM (central AGN, galaxies, stars). The arc-shaped brighter excess regions arise from the sloshing process.

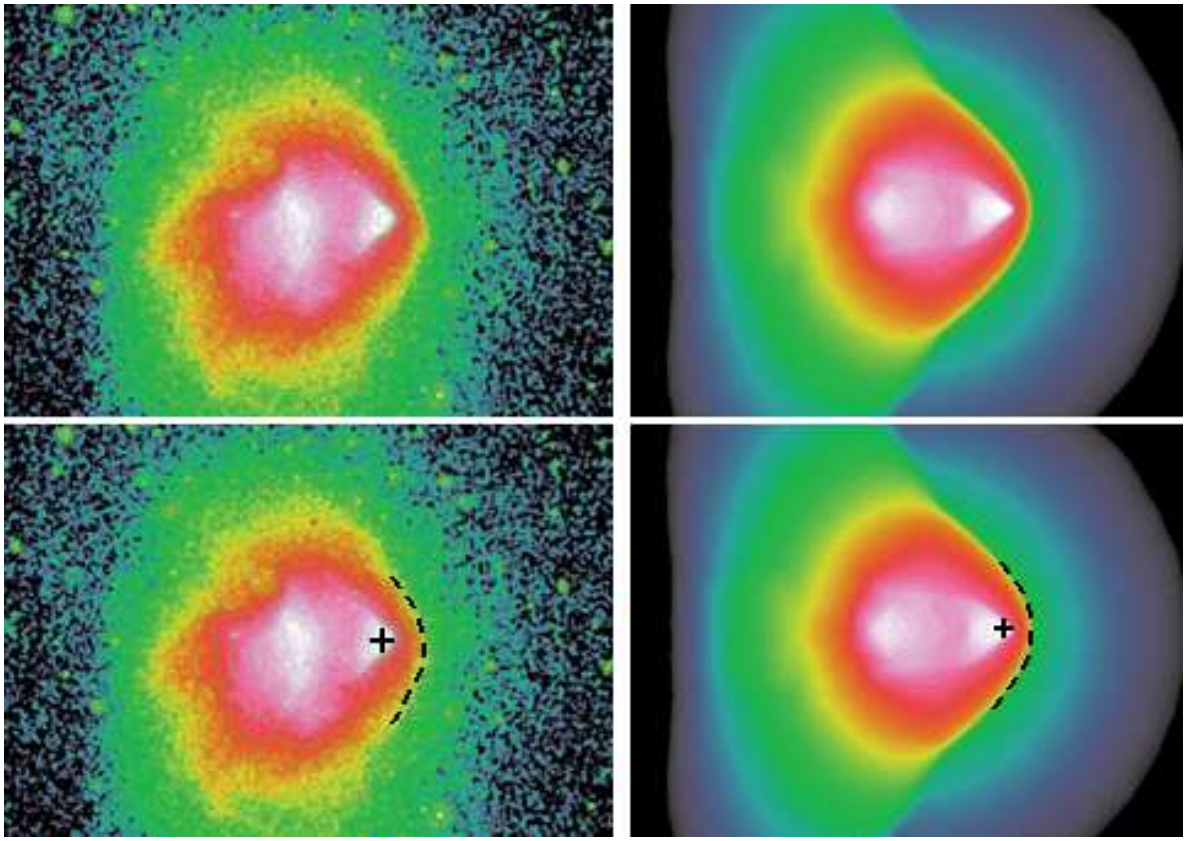

Figure 1.3: X-ray observations of 1E0657-56, the *'Bullet cluster'* (figure 2; Springel & Farrar, 2007). The left column features an X-ray observation from Chandra, whereas the right column shows mock observations of a simulated merger closely matched to the bullet cluster. The images show X-ray brightness, indicated via the colour scale, from white, highest, to black, lowest. In the bottom images, the cross corresponds to the epitomous 'bullet' of the Bullet cluster, the blunt gas halo of the infalling subcluster. The black dashed line corresponds to the bow shock generated by the supersonic motion of the infaller (See figure 2.2 for more detailed bow shock anatomy).

real one.

Not all mergers are created equal, and when observing, or modelling, galaxy cluster mergers problems can arise. Difficulties regarding complex morphology are readily apparent in the case of A520. A520's ICM is also comparatively 'hot': with X-ray emission peaks between 6.3 – 13.5 keV (Mahdavi et al., 2007), depending which region of the cluster we are concerned with. In their study, Wang et al. (2018) used a deep 0.5 Ms Chandra observation of the galaxy cluster (Wang et al. 2016), to examine a bow shock in the merging cluster. They used Rankine-Hugoniot jump conditions to estimate the Mach number of the infaller, finding a higher estimate than other studies based on shorter exposures. Emery et al. (2017) studied a

merger bow shock associated with a galaxy cluster around $3C438$, using a series of Chandra observations to build up a 166.9 ks merged image. The comparatively lower merger mass is reflected in the far more muted X-ray images of the cluster. As a final example, Tanaka et al. (2010) studied Abel 85 via $\sim$ 100 ks observations from Suzaku. Finding a hot spot not readily explained by previous studies, they suggested the subcluster is merging from the 'southeast' direction (figure 10). Instead, they treated the hot spot as an indicator of a shock wave formed from a 'southwestern' direction. Making use of Rankine-Hugoniot jump conditions, they estimated infall velocity based on this alternative hot spot and merger direction interpretation. Considering a 'postshock' region evidence of merging from the southwest in contrast to prior studies.

1.4 Thesis Aims

The objective of this thesis is to assess the limitations of Rankine-Hugoniot jump conditions for estimating the infall velocity of a subcluster during a minor merger. We do so via analysis of a hydrodynamic + N-body simulation of a minor 1:10 galaxy cluster merger. To this end, we will proceed as follows: in the next section, chapter 2, we describe the physics of bow shocks and Rankine-Hugoniot jump conditions. Following this, we detail our specific simulation, host and infaller DM treatment, alongside the approach used to measure the infaller velocity in chapter 3. The latter includes measuring the infaller velocity from RHJCs and it's 'true' velocity from the simulation's raw data. Chapter 4 covers the main results of our investigation, with chapter 5 containing the relevant discussion. We discuss the strengths, and weaknesses, of Rankine-Hugoniot infall velocity estimates during different phases of our minor merger simulation. Concluding with chapter 6, we summarise the thesis as a whole. Additionally, we provide some suggestions for further study, including specifics for improving infall velocity measurements based on the experiences of this thesis.

2. Bow Shocks

Bow shocks are arc-shaped shocks ahead of objects travelling supersonically through a gas or fluid. Here we summarise the essential physics of bow shocks, and connect these to the minor merger scenario. In particular, we describe the Rankine-Hugoniot jump conditions that relate the ratios of density, temperature, and pressure across a shock to the shock's speed.

2.1 Characterising Bow Shocks

First, we consider the simple case of the motion of an object with constant velocity through a homogenous fluid. For a given medium, through which an object passes, particles of the medium are deflected around the object as it travels. The shape, velocity, and other properties, of the object dictate the manner in which this deflection occurs. We consider the 'flow' of a fluid around an object in several regimes, dependant on the relative velocity between our object and the speed of sound in the fluid. We express the ratio of these two velocities as a Mach number, defined as the ratio of flow velocity, v, to the ambient medium's speed of sound, c:

$$M = \frac{v}{c}, \tag{2.1}$$

We broadly categorise this relative motion as subsonic, transonic, and *supersonic*. We consider an object to be travelling supersonically if the object's speed with respect to the undisturbed upstream fluid is faster than c. In the case of supersonic motion, pressure waves of deflected particles generated by this motion are compressed into a single discontinuity ahead of the object, a shock wave or shock (Anderson, 2011).

In figure 2.1, we can see two bow shocks captured via shadowgraph imaging. Both images show a 'bow' shaped discontinuity ahead of the blunt spheres known as a *bow shock*, visible as a dark black line ahead of each. At the shock, there is a discontinuous change in pressure, density, and temperature of the medium (Paterson, 1983). The gap ahead of both

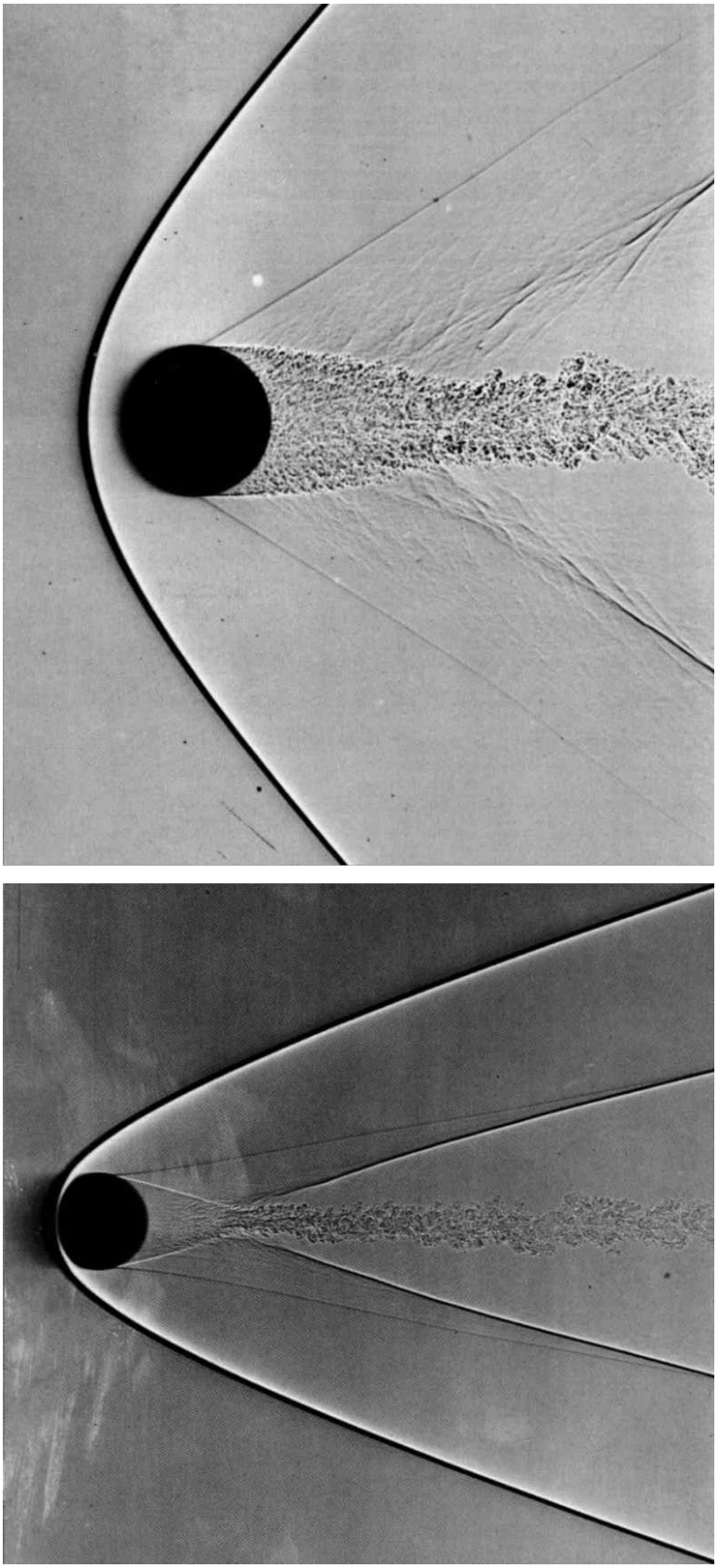

Figure 2.1: Two shadowgraph images showing 1/2 inch spheres travelling in free flight through air, the top and bottom spheres are travelling at travelling at Mach 1.53 and 4.01, respectively (Van Dyke, 1982).

spheres, between the shock discontinuity and the edge of each sphere, is referred to as the 'standoff distance'. The shape of the sphere, and the consequent angle of deflection, results in a subsonic 'cushion' of the flowing medium forming ahead of the sphere. At the poles of the spheres, we can see a secondary oblique shock attached. Turbulent wakes behind the spheres generate weak disturbances, later merging into the oblique shock wave (Van Dyke, 1982). The relative velocity difference between the spheres and the air impacts the structure of the bow shock. At lower Mach numbers, top image, the bow shock is wider and more spread out. The standoff distance is larger and the secondary shock is close to the vertical axis of the sphere. Conversely, in the bottom image, the bow shock has a smaller opening angle and the standoff distance is much smaller. The primary bow shock, and secondary shock, are much more swept back. The increased velocity has resulted in the wake of the sphere generating another shock which merges with the oblique shock downstream. Bow shocks, like those in figure 2.1, are common features in aerodynamics and hydrodynamics. From spacecraft re-entering the Earth's atmosphere, to shocks within merging galaxy clusters, bow shocks are found throughout the universe (e.g. Billig, 1967; Schulreich & Breitschwerdt, 2011).

The ICM is an ionised plasma permeated by a weak magnetic field. At the scale of galaxy cluster mergers, contributions from thermal pressure are much greater than those from magnetic pressure (ZuHone & Roediger, 2016). We therefore describe the ICM with hydrodynamics, neglecting magnetic fields, in line with many other works. By treating the ICM as an ideal, hydrodynamic fluid, the relationship between matter on each side of a bow shock, such as those formed by an infalling subcluster in a galaxy cluster merger, can be used to inform velocity estimates for an infaller.

In a galaxy cluster merger, the infaller's gaseous core is comprised of dense, gravitationally bound gas at the pit of the infaller's potential well. This relatively denser, cooler gas, serves as the obstacle to the ambient ICM flow much like the spheres pictured in figure 2.1, constituting the remains of the infaller's ICM and galactic atmosphere. The infaller's gaseous core acts as a 'blunt body' of sorts, providing the structure required to drive a bow shock ahead of it and through the host cluster's ICM. There are, however, differences to the solid spheres.

Ram pressure stripping progressively whittles away the atmosphere of the infaller (Roediger et al., 2015a). Shear velocity at the boundary between ICM and infaller atmosphere induces Kelvin-Helmholtz instabilities, stripping further gas away from the merging subcluster (Livio et al., 1980; Nulsen & Fabian, 1980; Roediger et al., 2015b). Thus, instead of an obstacle of constant size, the gaseous atmosphere of the infaller forms an obstacle that shrinks in size over time. Even with mass ratios as high as 1:10, the Bullet cluster and other simulation based studies demonstrate that infallers involved can survive a first infall period, provided the angle of impact is not too low (Markevitch et al., 2002; Sheardown et al., 2019; Vaezzadeh et al., 2022).

Once the merging subcluster is moving fast enough, relative to the ambient ICM, a bow shock forms. In figure 2.2, we see a breakdown of the varying components that make up our bow shock system. We can consider gas to be 'shocked' once it has been overrun by the bow shock, or 'unshocked' if it is yet to be. Unshocked gas has the properties of the host cluster's ICM, in terms of pressure, density, and temperature. If the gas is shocked, then these values increase. The stagnation point is the position where, in the rest frame of the infaller, the flow velocity from upstream gas is zero (Vikhlinin et al., 2001; Fish, 2020).

Bow shocks in merging clusters can be considered roughly analogous to their terrestrial counterparts, provided we make some important distinctions. We discussed above that in the case of a cluster merger the 'obstacle' to the flow shrinks, whereas in classic terrestrial examples the obstacle is constant in size. The second point concerns the homogeneity of the ambient medium. In most terrestrial examples, the unshocked air that the object in question travels through is homogeneous on spatial scales comparable to the bow shock extent, i.e., over 10s of object diameters, the air is of constant density and temperature. This is not the case in galaxy cluster mergers. A subcluster atmosphere of 10s of kpc drives a shock of 100s of kpc in size, i.e., a size comparable to the host cluster. On scales of 100s of kpc, the host cluster's ICM is not homogenous, but varies dramatically. On such scales, the temperature of the ICM varies by roughly one magnitude, whereas density and pressure gradients can range over three or more magnitudes (Mohr et al., 1999; Markevitch et al., 2002). The changing velocity of the subcluster must also be considered. Pre-pericenter passage we can consider the infaller

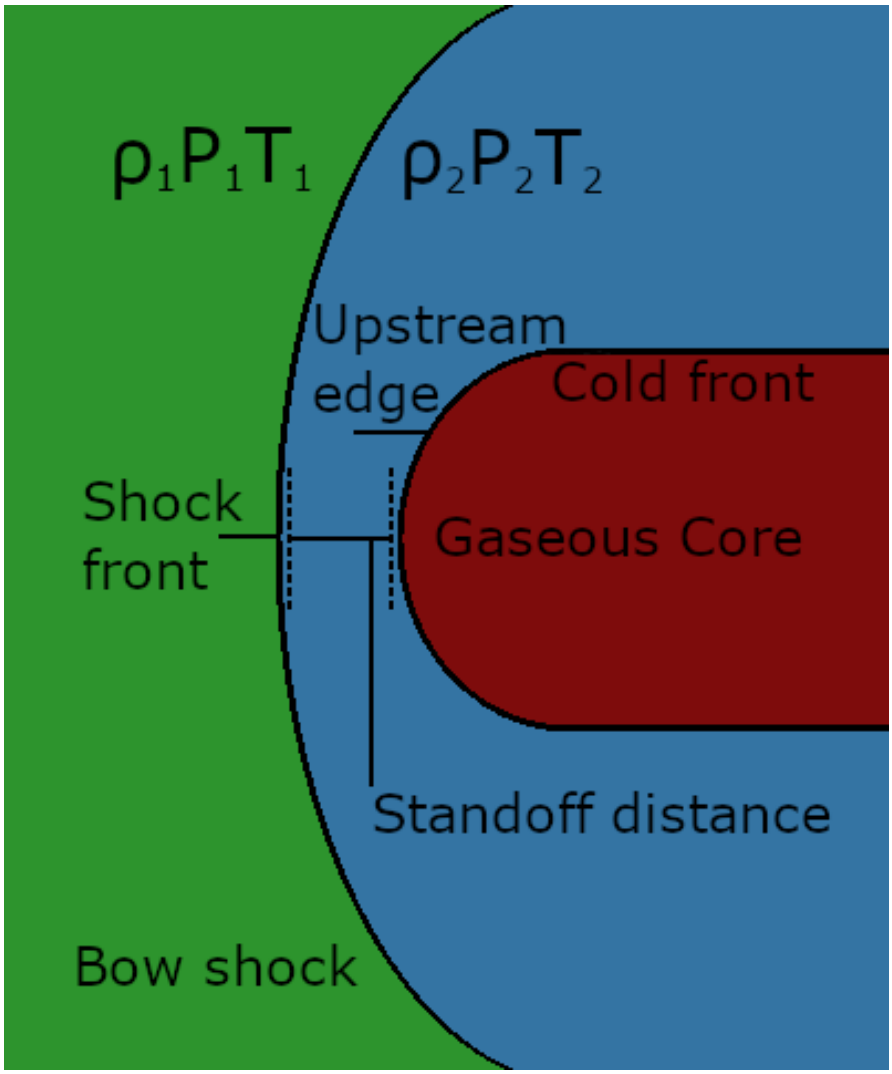

Figure 2.2: A diagram showing the anatomy of an infalling subcluster driving a bow shock, sketched from a single frame of our simulation. The colour scheme corresponds to the ICM, indicating the different origins of the gas. Green and blue are the host cluster's ICM, representing unshocked and shocked states, respectively. Dark red is the remaining ICM or atmosphere of the infalling subcluster, the 'gaseous core' of the infaller. This core is wrapped in a contact discontinuity, known as a cold front, separating the atmospheric ICM of host and infaller. The bow shock, being driven by the subcluster, is visible as the separation between the unshocked and shocked ICM. Standoff distance is the distance between the gaseous infaller core and the bow shock, the point of the shock closest to the core. The unshocked and shocked ICM gas has different properties either side of the discontinuity, denoted by subscript 1 and 2 (Su et al., 2017; Zhang et al., 2019a).

to be accelerating, reaching maximum velocity around pericenter passage. Post-pericenter passage, shocks are not subject to the same deceleration as the infalling subcluster. The steep density and pressure gradients allow bow shocks to 'run away' as the infaller decelerates. Atmospheric shocks lose energy and momentum for each unit distance travelled, conversely a merger shock expends less and less energy at greater r. Once no longer driven by an infaller, the driven shock detaches and slides down the cluster ICM gradient, propagating outwards towards the cluster's periphery. At this stage shock velocity bears no connection to subcluster velocity. Beyond a critical radius, shock velocity can be maintained for some time, perhaps indefinitely (Zhang et al., 2019b; Zhang et al., 2021).

2.2 Sound Speed

When examining galaxy cluster mergers, we use the frame of reference in which the host cluster is 'stationary'. Thus, all other motion is discussed relative to the larger cluster. Generally, we refer to the speed of sound in the ICM as the 'ambient sound speed'. To make our infall velocity estimate, we begin with the ambient sound speed of the ICM. The speed of sound in an ideal gas, is given via the Newton-Laplace equation:

$$c = \sqrt{\gamma \frac{P_1}{\rho_1}}, \tag{2.2}$$

Using notation as in Landau & Lifshitz (1987), Russell et al. (2010), and Su et al. (2017), here subscript 1 denotes unshocked gas. The ICM can be described as a monoatomic gas thus, we use $\gamma = 5/3$. P and ρ indicate pressure and density, respectively. The Rankine-Hugoniot conditions below relate the Mach number of the shock to the density, temperature, or pressure ratios across the shock. The Rankine-Hugoniot derived Mach number multiplied with the sound speed gives the shock speed.

2.3 Rankine-Hugoniot Jump Conditions

So named after the Scottish and French engineers, these jump conditions, relate states of matter on each side of a shock wave to the speed of the shock. Principally, energy, momentum, and mass must be conserved across the shock (Landau & Lifshitz, 1987). If we can measure

matter conditions on both sides of the shock wave, we can determine the speed of the shock. In our case, we take gas just ahead of the bow shock which is unshocked and the shocked gas to be the gas conditions directly behind the bow shock. According to Rankine-Hugoniot jump conditions (see: Landau & Lifshitz, 1987, also Russell et al., 2010), the Mach number of a shock relates to the pre- and post-shock conditions via the following derived relationships:

$$M_t = [\frac{(\gamma+1)^2(\frac{T_2}{T_1}-1)}{2\gamma(\gamma-1)}]^{\frac{1}{2}}, \tag{2.3}$$

$$M_\rho = [\frac{2\frac{\rho_2}{\rho_1}}{\gamma+1-\frac{\rho_2}{\rho_1}(\gamma-1)}]^{\frac{1}{2}}, \tag{2.4}$$

Here T_2 and ρ_2 are the temperature and density of the shocked gas immediately downstream of the shock, whereas T_1 and ρ_1 is the unshocked for temperature and density, $\gamma = 5/3$ for ICM, respectively. We differentiated between Mach numbers derived from the temperature and density jumps, M_t and M_ρ. Whilst these values should be the same, we will see that results can differ. Certain conditions are assumed whilst using the Rankine-Hugoniot equations:

- The shock is planar and is perpendicular to the flow speed, i.e., the shock is not oblique
- The shock speed is constant
- The upstream conditions are homogenous

Our discussions of bow shocks in clusters makes clear that the underlying assumptions for the Rankine-Hugoniot jump conditions are not fulfilled in cluster bow shocks. Bow shocks are curved, the shock speed changes over time, and the upstream conditions are not homogenous. In the past, Rankine-Hugoniot jump conditions have still been applied to cluster bow shocks, specifically to the jumps in T and ρ at the bow shock. The goal of this thesis is to determine how good an estimate for the subcluster infall speed the Rankine-Hugoniot jump conditions allow.

3. Methodology

For this thesis, we analyse Rankine-Hugoniot jump conditions by way of 'observing' a simulated galaxy cluster merger. We utilise an idealised simulated binary minor merger, with a mass ratio of 1:10. This simulation was the work of, and described in detail by, Vaezzadeh et al. (2022). We focus our simulation analysis on the initial 5 Gyrs. This covers the subcluster's first and second infall. In this chapter we discuss the simulation specifics, the definitions used, how Rankine-Hugoniot jump conditions are applied, and how the subcluster velocity is measured.

3.1 Binary Merger Simulations

3.1.1 Simulation Setup and Initial Conditions

Our simulated idealised 1:10 minor merger uses generic galaxy clusters. The host cluster and infalling subcluster possess masses 5×10^{14} $M_\odot$ and 5×10^{13} $M_\odot$, respectively. Using the approach of ZuHone (2011), the simulated galaxy clusters are spherically symmetrical, self-gravitating, and in hydrostatic equilibrium. Both cluster potentials are modelled by a spherical Hernquist profile (equation 3.1, Hernquist, 1990), whereas the ICM is treated as an ideal gas using a Cavaliere & Fusco-Femiano (1976) standard β profile that is truncated at large radii (equation 3.2).

$$\rho_{\text{total}}(r) = \frac{M_{\text{total}}}{2\pi} \frac{a}{r(r+a)^3}, \tag{3.1}$$

$$\rho_{\text{ICM}}(r) = \rho_0 \left(1 + \left(\frac{r}{r_{\text{c}}}\right)^2\right)^{-\frac{3\beta}{2}} \left(1 + \left(\frac{r}{r_{\text{cut}}}\right)^3\right)^{-1}, \tag{3.2}$$

Where M_{total} and a denote total mass and scale radius. For the host cluster and subcluster, we use $a = 566$ and $a = 230$, respectively. r_{c} is core radius, and r_{cut} is the truncation set at

2783 kpc. β is set to 0.64, an approximate value determined via detailed X-ray flux study of 45 galaxy clusters (Mohr et al., 1999). The DM density of the merging clusters is the difference between total density and the β profile. The simulation's box boundary condition is periodic, minimising long-term boundary effects on the model. The masses, and subsequent temperatures, of the clusters were chosen to be representative of an average cluster for the host cluster, and a small cluster for the merging cluster. Further rationale and implications of these settings are discussed in detail in Vaezzadeh et al. (2022). The simulation phase considered in this thesis covers initial conditions, $t = 0$, until $t \simeq 5$ Gyr, with each simulation output, or frame, stored in intervals of 50 Myr. Here, the infaller completes three infall periods, with the infalling subcluster's gas halo merging with the host at the end of third infall period. Due to dynamic friction, the infaller has slowed down to subsonic speeds by this point, thus, does not drive a bow shock any more.

The merging clusters are initially separated by $\sim$ 2400 kpc, with the host cluster positioned at $x = 0$ and the infalling subcluster at $x = 2397$ kpc. The y and z components start at 0 kpc for both clusters. This distance is equal to the combined r_{200} radii of the respective clusters, used in substitution for the virial radius of the galaxy clusters (see: Opher, 1998). The infalling subcluster also possesses initial velocities $v_{\rm x} = -966$ and $v_{\rm y} = -299$ km s^{-1}. The tangential velocity, $v_{\rm y}$, is set such that the infalling subcluster reaches a certain pericenter distance (closest orbital approach) from the host cluster and does not merge head-on. The initial velocity, $v_{\rm x}$, is based on cosmological simulations such that at r_{200} the infalling subcluster has a specific and realistic infall velocity. Both the initial separation and velocity are based on the works of Vitvitska et al. (2002).

3.1.2 FLASH Code

The simulation was run using FLASH, a modular adaptive mesh hydrodynamics code (Fryxell et al., 2000). Originally designed to study thermonuclear flashes in and on neutron stars, it has also found use in modelling galaxy cluster mergers to study a variety of features (e.g., ZuHone et al., 2010, Sheardown et al., 2018). Utilizing 3D hydrodynamic and N-body code enables accurate modelling of interactions between gaseous and collision-less matter (self-gravitating

particles: DM, galaxies). In turn, this allows us to capture the effects of dynamical friction and tidal forces, which influence the infalling subcluster's orbit and thus the merger evolution as a whole.

FLASH is a 'grid-based' code. Put simply, a grid code divides the spatial region to be simulated into small cubes called grid cells. The initial conditions set the density, pressure, temperature, and velocity of the gas in each grid cell. The code then calculates the motion of the fluid or gas in the simulation volume between the grid cells, according to the forces acting on the fluid, such as pressure gradients or gravity. FLASH's adaptive mesh alters the size of grid cells dynamically. A region of space with a greater grid cell density will possesses more resolution, consuming more computational resources. Therefore, the inner regions of the host and infalling clusters are modelled via many more grid cells, as opposed to those cells on the simulation's periphery. Spatial resolution varies between $3.7 - 25.4$ kpc, with the maximum resolution at the inner $250 - 125$ kpc of the clusters, host and subcluster, and the lowest at the edge of the 4 Mpc region of space we examine. This grid refinement takes place over the evolution of the simulation, applying to each specified simulation step. Further specifics, and more technical elements, can be found in Vaezzadeh et al. (2022).

3.2 Simulation Analysis

For analysing and extracting information from our simulation, we primarily use Python and the package 'yt' (Turk et al., 2011). yt is the main code used for exploring, retrieving, and visualising our simulation data. To evaluate Rankine-Hugoniot jump conditions for the subcluster velocity we require the following data from the simulation: (i) unshocked ICM density and temperature, (ii) shocked ICM density and temperature, (iii) the velocities of the host, subcluster, and shock, (iv) the ambient sound speed of the unshocked gas. Below, we describe how these pieces of information are retrieved from the simulation.

3.2.1 ICM Profiles Across the Bow Shock

To begin, we determine orbital positions for both the host cluster and the infalling subcluster. We define the host cluster, and infaller, position as the location of their DM density peaks.

In practice, the peak DM density position for the entire grid marks the host's center. By excluding a sphere of radius 70 kpc around the host's center we find the infaller's DM peak. We tested defining the host and infaller center locations using their ICM density peaks. During first infall, the separation of the subcluster's DM and ICM peak is at most $\sim$ 4 kpc, at $\sim$ 1300 Myr prior to pericenter. Prior to second pericenter passage, ICM-DM separation increases rapidly, coinciding with the infaller gas halo stripping. Both cluster center identifications were visually inspected and identified correctly in all relevant time frames using slice images, like in figure 3.1.

Both the host cluster and infalling subcluster, DM and gas, positions are stored for each simulation frame, tracking their motion throughout the evolution of the merger. For each time frame, we then extract a profile of gas density and temperature across the bow shock. Using the infalling subcluster's current position as an origin point, we draw a ray (YTRay) 750 kpc long in the subcluster's direction of motion. This direction of motion is identified by via the subcluster's position in the next simulation frame. The ray intersects the infalling subcluster's position in the next simulation frame, thus passing through the bow shock in the current time step. An example of a ray can be seen in figure 3.1. The ray itself is denoted by the white line, starting at the infalling subcluster center indicated by the white cross. The principle job of this ray is to extract gas data from the simulation and store it. We are interested in the gas temperature and density along our ray, using these values to calculate our ambient sound speeds and the desired Mach numbers.

To determine the Mach number and infall velocity of the subcluster, we use the ambient sound speed of the ICM as is in equation 2.2. Given the dynamic situation of the ongoing merger and the spatial variation of ICM density and temperature even at initial conditions, the difficulty lies in determining from where to extract unshocked gas data. In our case we use the unshocked conditions directly upstream of the bow shock from the forward ray profiles described above. The temperature and density profile of the gas sampled by the ray, figure 3.1, is visible in figure 3.2. The FLASH code will 'smooth out' discontinuities over $\sim$ 4 grid cells, hence we set the 'Unshocked gas' position equal to 'Shock position' +4 grid cells. This ensures that, for each frame of the simulation, we are evaluating the unshocked gas just ahead

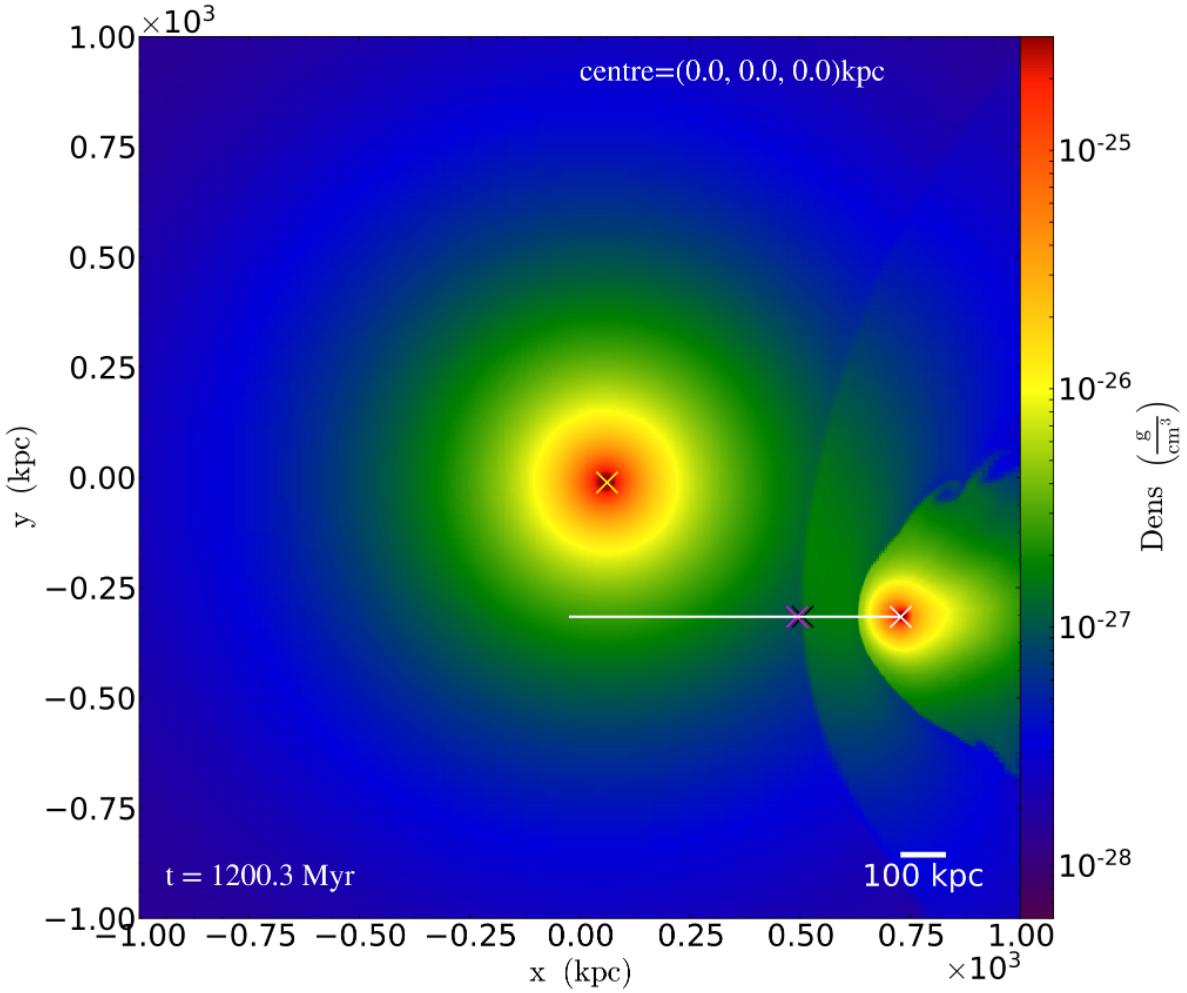

Figure 3.1: A density slice of the simulation at 1200 Myrs, companion graphic to figure 3.2. The white line represents the ray in this time step, along which we gather gas data. The coloured crosses correspond to positions important to the process of assessing gas properties. The yellow cross marks the host cluster's center in the current time step, whereas the white cross corresponds to the infalling subcluster's center. The black cross along the ray-line corresponds to 'Shock position', marking the spatial position of the bow shock. Ahead of this, the magenta cross marks the location +4 grid cells ahead of the bow shock's 'Shock position', which we refer to as the 'Unshocked gas'. This position depends on the simulation's refinement level at, and around, the bow shock. Consequently, the gap between the black 'Shock position' and magenta 'Unshocked gas' position is largest during the early stages of the merger, when the bow shock is on the cluster periphery.

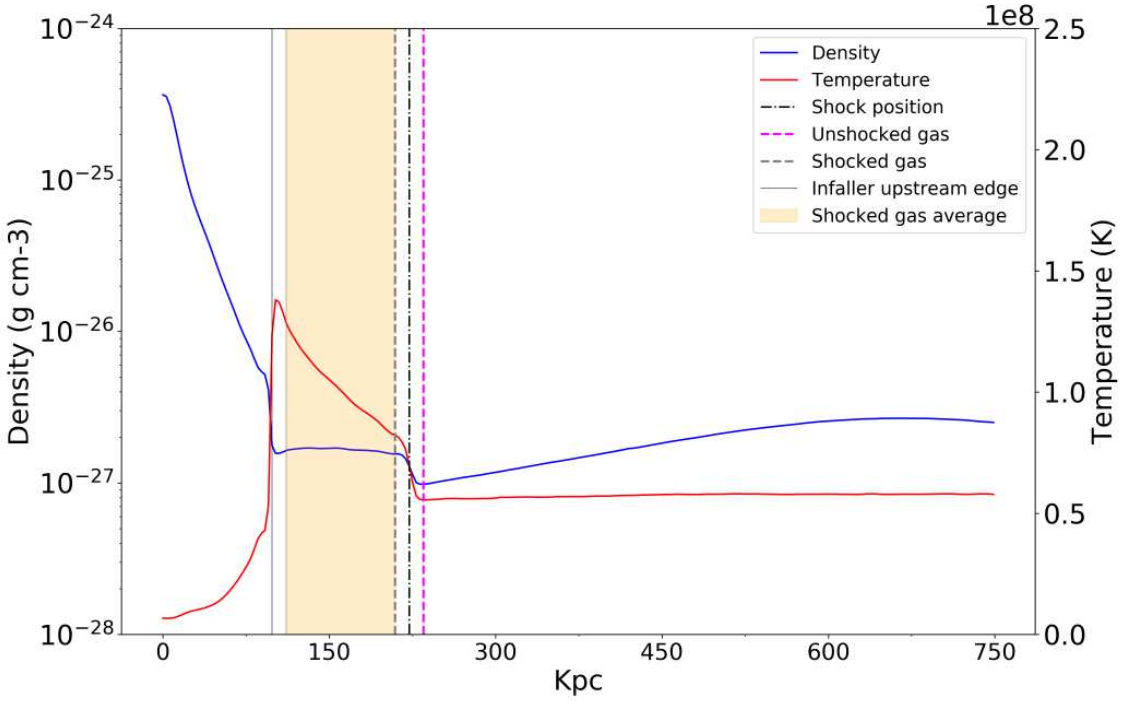

Figure 3.2: Gas profile across the infaller's bow shock at 1200 Myrs, representing the data extracted along the ray shown in figure 3.1. The solid blue and red lines show the ICM density and temperature profile, respectively. The black and magenta vertical lines correspond to their similarly coloured marks on the ray, representing 'Shock position' and 'Unshocked gas', respectively. The vertical grey and magenta lines, representing 'Shocked gas' and 'Unshocked gas', are ±4 grid cells of 'Shock position' and show the values we use for applying Rankine-Hugoniot jump conditions in this simulation frame (equations: 2.3 and 2.4). 'Shock position' is determined by way of temperature gradients, using the steepest gas profile increase position. The yellow shaded area represents the selection of data used when producing 'Average' Mach numbers.

of the bow shock, which we then insert into equation 2.2.

Having determined the sound speed of the local ICM, we can now extract the Mach number, and subsequent speed, of the infalling subcluster using Rankine-Hugoniot jump conditions. We use two methods to extract the shocked gas temperature and density.

The 'point' method extracts the density and temperature at a single point in the shocked gas profile, again 4 grid cells away, downstream of the shock position (See figure 3.2). In real observations it is impossible to measure the ICM properties of such a small region, consequently we test an alternative method. Here we average the density and temperature in the forward ray profile between the shock and infaller's upstream edge. We refer to this approach as 'average'. With shocked and unshocked density and temperature known, we can calculate Mach number using density and temperature jumps according to equations 2.3 and 2.4. As the ambient sound speed of the unshocked gas is known, we can convert Mach numbers to infaller velocity estimates. Using this method, we measure the Mach number and speed of the infalling subcluster purely from ICM "observations".

3.2.2 Simulation Comparator Mach Numbers

The remaining task is to extract from the simulation the "true" velocity of the infaller in this scenario. For both the infaller and host cluster, we measure the velocity of the gas and DM halos. Using the change in position of maximum ICM density or particle density over the 50 Myr between frames, we take this as the velocity of the subcluster's gas and DM halo, respectively. We repeat this process for the host cluster's DM halo, recording the change in position of the core and using the derived velocity to correct the infaller with respect to the host. We also produce a gas halo velocity by way of gas bulk velocity. For this process, we evaluate all simulation cells contained within a sphere, of given radius $r = 7.5$ kpc, to determine the average velocity of the gas contained therein. In our case, using the infaller's current position we define a sphere of $r_{7.5}$ and extract the bulk velocity of the gas. Correcting this new value relative to a similar $r_{7.5}$ gas bulk velocity of the host cluster gives us another infall velocity approximation.

Our usage of Rankine-Hugoniot jump conditions to determine velocity of the infalling

subcluster relies on the assumption that the shock velocity is equal to the velocity of the driving body. Given the rapid change in size of the infaller's gas halo, caused by gas stripping, this assumption is not always true. To assess the importance of this effect we track the motion of the 'Shock position' marker, as determined from the forward ray, throughout the evolution of the merger. From this motion between time frames, we derive the shock velocity. We correct the shock velocity for the velocity of the host center, i.e., derive the shock speed with respect to the host cluster. Finally, we produce one more measure of shock velocity, namely the shock speed relative to the ICM bulk velocity upstream of the shock. To this end, we measure the bulk velocity in a sphere of radius 7.5 kpc at 50 kpc ahead of the bow shock. Thus, we have three reference frames to compare the Rankine-Hugoniot derived infaller or shock velocity to: (i) velocity of infaller center with respect to host center, (ii) velocity of the bow shock, defined as 'Shock position' on the forward ray, with respect to host center, (iii) velocity of the bow shock with respect to the ICM upstream of it.

4. Results

4.1 Epochs with Bow Shocks

Prior to applying Rankine-Hugoniot jump conditions, we confirmed bow shock presence, and thus the suitable simulation frames, via slice images as in figure 3.1. These slices covered the entire simulated merger evolution, some $\sim$ 5300 Myrs. Visual inspection identified bow shocks during two distinct intervals, formed during first and second infall, and therefore suitable frames to apply Rankine-Hugoniot jump conditions. The bow shock presence in these intervals is confirmed in our ray ICM profiles as characteristic discontinuities in density and temperature. The first bow shock is measurable between simulation times $100 - 2050$ Myrs, whereas the second bow shock is present between $3950 - 4300$ Myrs. These time frames are referred to as 'first' and 'second' infall, respectively even thought the first epoch contains the subcluster's motion from pericenter to apocenter. We identified a third infall period via mass density slices, but no bow shock forms as the infaller gas halo has since fallen into the host, leaving only the DM remaining to complete infall. Consequently, there are no measurements and data for this period.

Our slices and profiles showed us a stark difference in shock lifetime. During second infall, the driven bow shock is visible for less than half the time of the first. We found that on second infall the bow shock was visible and driven only for $\sim$ 400 Myrs. In contrast, during the first infall the bow shock is visible as early as 100 Myrs into the simulation as the simulation start with a supersonic infall. The bow shock is present and driven by the infaller for $\sim$ 2000 Myrs.

4.2 Applied Rankine-Hugoniot Jump Conditions

Having determined shocked and unshocked ICM densities as described in the previous chapter, we are ready to apply Rankine-Hugoniot jump conditions to calculate the infaller's Mach

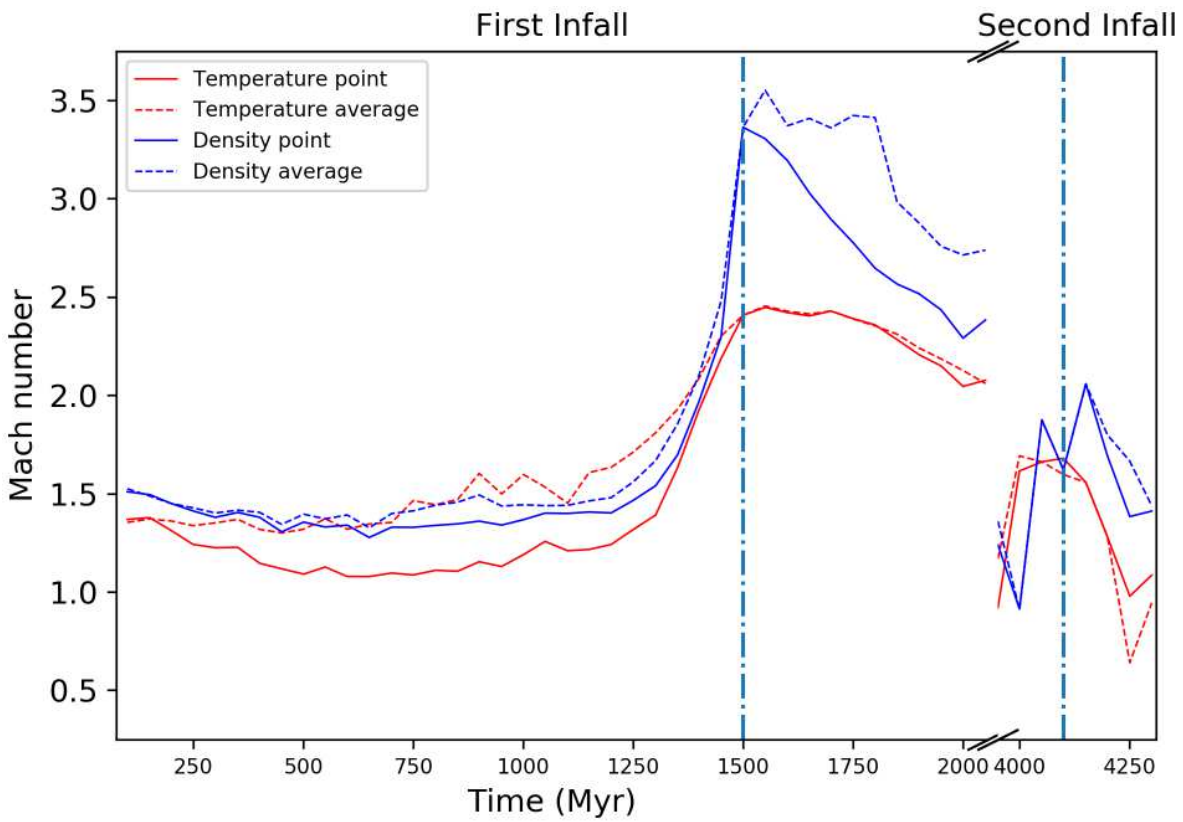

Figure 4.1: Subcluster Mach number against time for first and second infall as derived from Rankine-Hugoniot jump conditions. Line colour indicates Rankine-Hugoniot variable used, temperature or density, with solid and dashed style corresponding to point and average approaches, respectively (section 3.2.1). The cyan vertical dash-dotted line represents pericenter passage at 1500 and 4150 Myrs, respectively. Note the time axis is broken between first and second infall.

numbers according to equations 2.3 and 2.4. The results for both intervals with bow shocks are shown in figure 4.1.

At a glance, no Mach number recorded, for each approach, resembles another *precisely*. Instead, there are groupings and trends. Concerning first infall, Mach numbers are roughly grouped with the exception of temperature 'point', which diverges at $\sim$ 200 Myrs until pericenter passage at 1500 Myrs. The temperature based Mach numbers re-converge post-pericenter passage, presenting similar values and trending downwards until first cluster passage concludes. Conversely, density Mach numbers tend to occupy similar values up until pericenter passage, at which stage we see a divergence between density 'point' and 'average' Mach numbers. Post-pericenter passage, the differing ICM variables return Mach numbers with much wider differences and gradients. Temperature reports a much more gradual decline in Mach

number, conversely density features a much stronger difference in value between 1500 – 2050 Myrs. Density is also internally inconsistent, with differing slopes and final values depending on data approach.

Second infall presents quite differently from the first, with a shorter bow shock lifetime reflected in the smaller available dataset. Both sets of Rankine-Hugoniot Mach numbers are noisier, occupying a larger range of values when compared to the same time period during first infall. Whilst the data is noisier, the values reported appear to be more similar to one another pre and post-pericenter passage, compared to first infall. That said, we see similar final post-pericenter value and trend differences in Mach number between variables. Though the temperature Mach numbers reported at 4250 Myrs appear to be subsonic, which given the existence of the bow shock in that frame appears to be an 'unphysical' description. As final general observations, regardless of variable or approach Mach number peaks at, or +50 Myrs of, pericenter passage. Additionally, density consistently reports Mach numbers larger than the temperature equivalent. This is especially pronounced post-pericenter passage, with a ceiling difference of $\sim$ +1 M.

4.3 Simulation Comparators and 'True' Velocity

As discussed in section 3.2.2, we require measurements of the 'true' infaller Mach number in order to make meaningful comparisons against. We measured the Mach number of the infaller DM and gas halo, as well as of the shock with respect to upstream ICM velocity. These results are shown in figure 4.2.

During first infall we can observe two groupings, the DM-gas halos and the shock itself. Our measurements indicate that the infaller's gas halo is tightly bound to its DM halo. Conversely, our shock measurements report similar, albeit very noisy, Mach numbers to the halos up until $\sim$ 800 Myrs, after which there is a distinct separation. The shock Mach number remains constant until $\sim$ 250 Myr prior to pericenter passage, whereas the halo Mach numbers increase. The Shock speed does not exactly trace the infaller speed. Additionally, the shock's Mach number begins rapidly climbing at roughly 1300 Myrs, in lieu of the more gradual increase like the halos over first infall. We see differing variable behaviours post-pericenter as

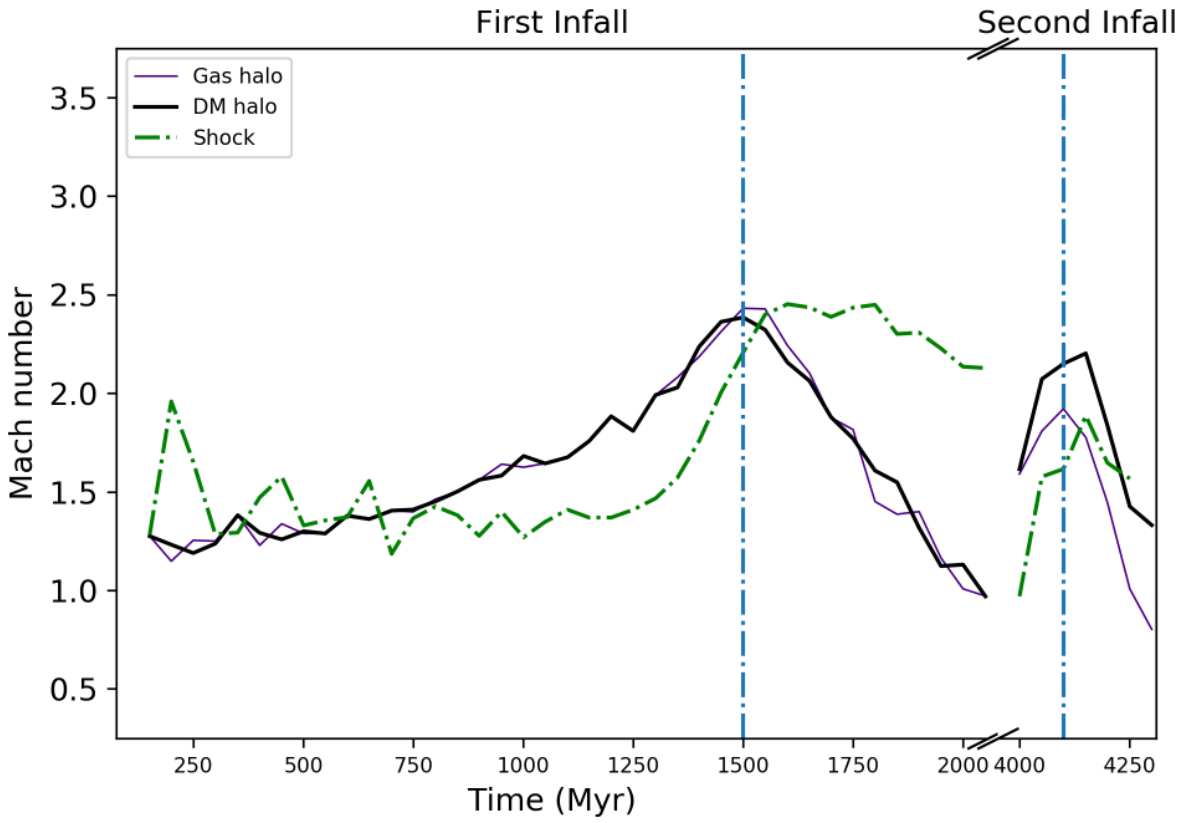

Figure 4.2: Infaller Mach number against time for first and second infall. Here we show the simulation-based infaller 'comparator' Mach numbers in isolation, to be compared against Rankine-Hugoniot Mach numbers in figure 4.3. At ~ 4300 Myrs the gas halo has lost much coherence, having previously glanced off much denser host cluster core gas, and is stripped. Consequently, whilst we can make accurate measurements of gas conditions either side of the shock, we cannot make precise distance measurements. As such, the 4300 Myr shock data point has been removed. Pericenter passage is indicated by the cyan vertical dash-dotted line at 1500 and 4150 Myrs.

well. With the shock peaking then losing ~ 0.25 M over 500 Myrs, in contrast to the stark and linear falloff of the halos from ~ 2.25 M to subsonic levels at 2050 Myrs. DM and gas halo values see increased variation but the Mach numbers reported are similar. We note the gas halo diverges from DM halo position by no more than 5 kpc pre-pericenter, but post-pericenter reaches a ceiling difference of 20 kpc at 1650 Myrs. This was verified visually, via slices, and measuring separation between the infaller DM / gas halo centers.

Concerning second infall, instead of two groupings we see three distinct Mach number evolutions. Both halos report similar initial values but quickly diverge pre-pericenter passage, with the gas halo consistently reporting a lower Mach number than the DM halo. Separation between the DM and gas halo increases linearly with time, with the host-infaller centers displacement increasing from just under 20 to in excess of 120 kpc over 200 Myrs. Here, the infaller is traversing an ICM over an order of magnitude denser, increasing the ram pressure exerted on the infaller's gas halo. Shock Mach number evolution resembles first infall, with a sharp rise through pericenter and peaking post-pericenter passage. There is a similar ~ 0.25 M depression in the post-pericenter shock Mach number, tapering off roughly 200 Myrs earlier when compared to first infall. The post-pericenter shock Mach number peak is about equivalent to gas halo peak, much like first infall.

4.4 Simulation Comparators versus Rankine-Hugoniot Mach Numbers

Having generated both Rankine-Hugoniot and comparator Mach numbers, these are shown alongside each other in figure 4.3. We can see from the outset that there are distinct groupings of variables, based on infall phase and whether it is pre or post-pericenter passage. Below we will describe the Mach number plot generally, during first and second infall, and finally bringing the ambient sound speed in later.

During first infall, whilst there is some noise for the first ~ 1000 Myrs pre-pericenter, we can see that the Mach numbers bear a general relation to one another. Between 250 – 750 Myr, the majority of our measurements cohabit the same Mach 1.35 – 1.50 band. Temperature point sits as the lowest predicted Mach number during this period. During 750 – 1250 Myrs, the Rankine-Hugoniot based values, as well as the shock, experience a reduced growth rate

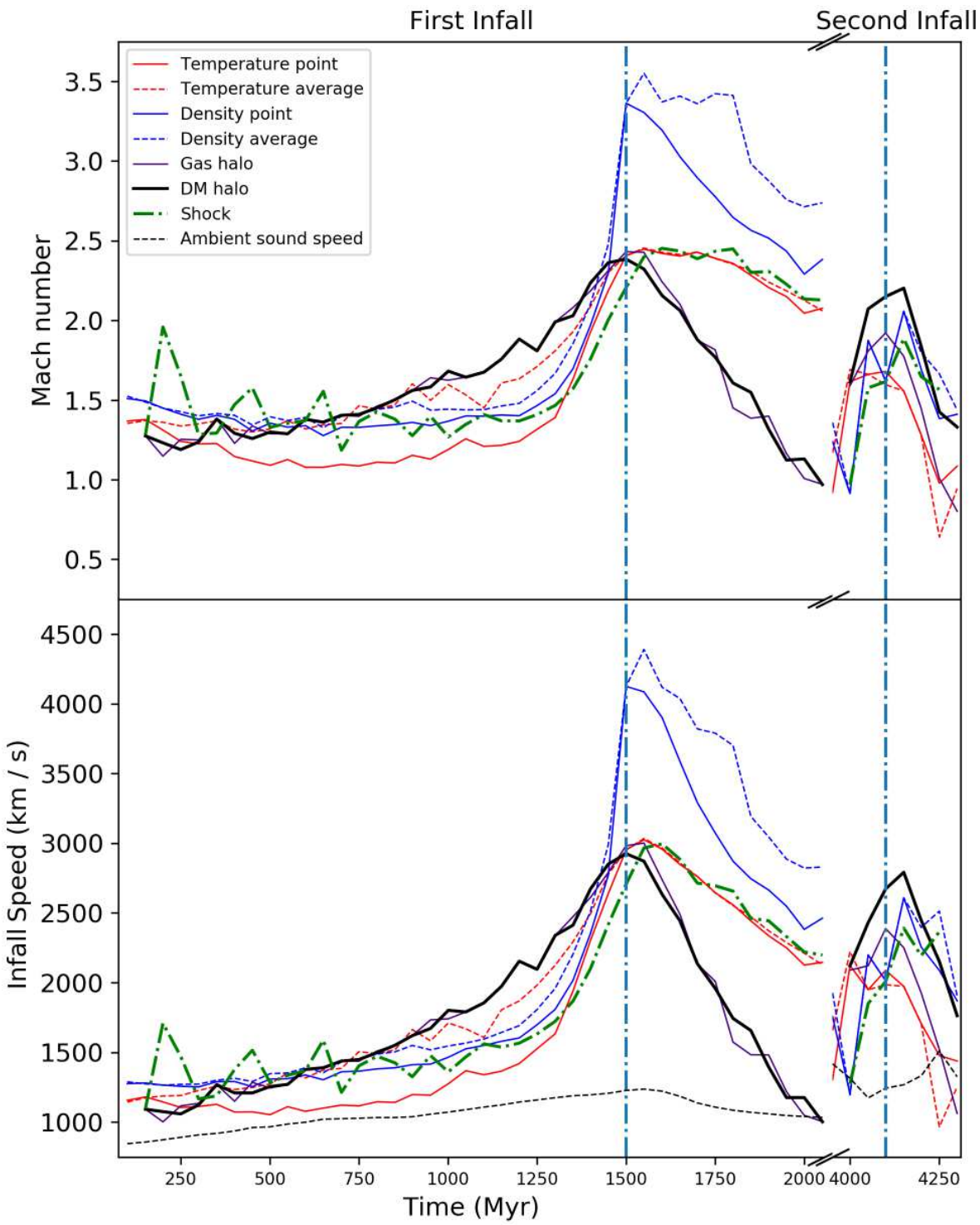

Figure 4.3: Mach number and infall speeds through first and second infall, showing Rankine-Hugoniot measurements alongside simulation comparators. The lower panel is a companion to the above Mach numbers plot, intended to contextualise the change in ICM ambient sound speed. The cyan vertical dash-dotted line represents pericenter passage during each infall phase, at 1500 and 4150 Myrs, respectively.

compared to the DM and gas halo Mach numbers. This changes between 1250 – 1500 Myrs. In the case of the temperature average Mach number evolution, it appears to bear the strongest resemblance to the DM and gas halo lines. Conversely, the temperature point measurements appear to make the weakest estimates. Notably point temperature diverges from this regime $\sim$ 200 Myrs into the simulation, from there it consistently underestimates the infaller Mach number. At pericenter passage, values appear to diverge into three distinct groups: i) density, ii) DM and gas halo, iii) temperature and shock. Density measurements of infaller Mach number appear grossly overestimated from pericenter passage onwards, even compared to the other Rankine-Hugoniot lines. The DM and gas halo lines continue being wound around each other, trending downwards and away from the other values. We discussed previously that post-pericenter the shock peaks then loses $\sim$ 0.25 Mach over 500 Myrs, this appears to hold true the for measured temperature values as well. The shock speed post-pericenter is clearly resembled by the temperature-based Mach number estimate.

With second infall, we see the same Mach number peaks at, or around, pericenter passage. The data is notably much more noisy than first infall, prohibiting judgement on smaller details. As soon as the DM and gas halo is available, temperature appears to make the best estimate pre-pericenter passage though it is not a strong resemblance. Post-pericenter, density appears to resemble a middle-ground between the shock and halos. Whilst temperature in this mode does not perform poorly, it does not perform as well as prior examples of temperature, regardless of whether point or average is used. The bottom panel of figure 4.3 shows the Mach numbers converted to speeds via the local sound speed. The variation of local sound speed with time is shown as well.

To better assess the relationship between the Rankine-Hugoniot derived Mach numbers against the DM halo and shock Mach numbers, we calculate the ratio of all Mach numbers to either the DM halo or the shock Mach number, shown in figure 4.4. We will discuss this plot in the context of first infall and then second infall.

During first infall, pre-pericenter the temperature average Rankine-Hugoniot estimate follows the DM halo speed within $\sim$ 15%. The density-based Rankine-Hugoniot Mach numbers trace the DM halo speed within $\sim$ 20%, the temperature-point estimate within

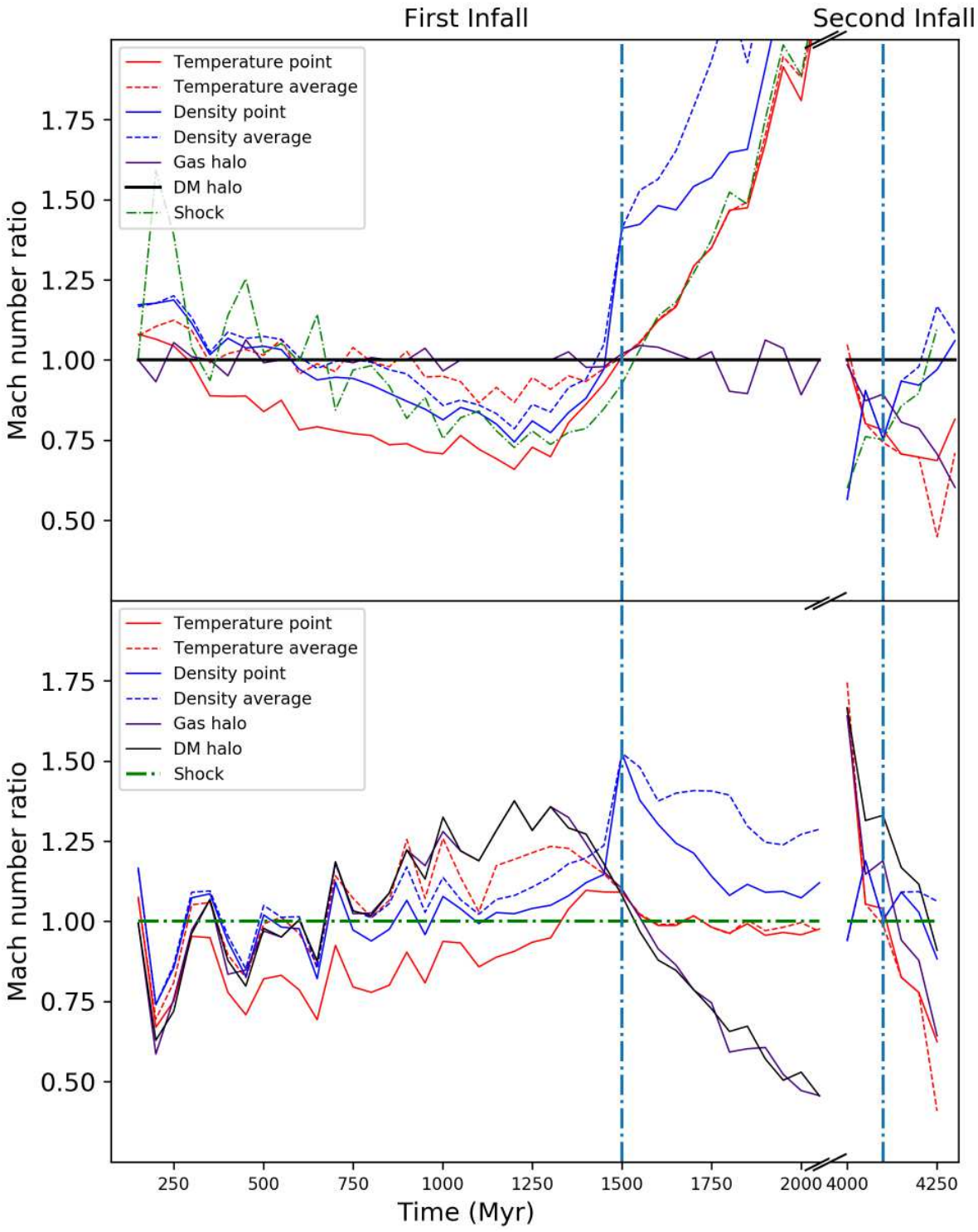

Figure 4.4: Mach number ratios between the infaller Rankine-Hugoniot and simulation comparator Mach numbers. All Mach numbers are divided by the DM halo (top) or the shock (bottom) Mach number, as indicated by the bold line at 1.00 M in the top and bottom plots, respectively. These plots have been zoomed to between 0.25 – 2.00 to better aid review. As before, pericenter passage is indicated by the vertical cyan dash-dotted line at 1500 and 4150 Myrs.

$\sim$ 30%. On the shock line we see the noise in the shock line, reflected in the 'yoyo-ing' in the values when set relative to the shock. Density Mach numbers appear to agree most with the shock's Mach number throughout pre-pericenter. Post-pericenter passage the DM and gas halos experience massive deceleration whilst other values reach their respective peaks. Here, temperature lines aligned with shock closer than gas DM halos above. We note that density appears more consistent than temperature during first infall, with a smaller difference between average and point data.

The behaviour of second infall warrants it's own consideration, as many of the earlier points raised regarding first infall no longer apply. In the right hand panes of figure 4.4 we see that, whilst noise is comparatively reduced versus figure 4.3, the data is still noisy but there are visible patterns and trends. Density-based estimates measure values between -40% to $+15\%$ and -10% to $+20\%$ of the DM halo and shock, respectively. Density-based estimates matching up well with the shock speed during second infall. Conversely, with values measured between $+5\%$ to in excess of -50% from DM halo, temperature-based estimates less correct than in first infall against both the DM halo and the shock. We can also see the increased separation between the DM and gas halos. Cross-referencing with figure 4.3, we see that all variables produce a subsonic measurement at some stage of the merger's evolution.

5. Discussion

5.1 Estimating Subcluster and Shock Speeds with Rankine-Hugoniot Jump Conditions in Different Merger Epochs

In this thesis, we have measured the orbital speed of a subcluster in a minor merger via a 3D hydrodynamic and N-body simulation by applying the Rankine-Hugoniot conditions to the subcluster's bow shock. Our objective was to discern the effectiveness and limits of the Rankine-Hugoniot jump conditions for estimating the subcluster's speed.

During the infall phases of the merger, i.e., while the subcluster is approaching the host cluster center, the Rankine-Hugoniot estimates come within 15 – 35% of the subcluster's actual speed. We defined the subcluster's actual speed to be the relative speed between the subcluster's and the host cluster's DM peaks. Post-pericenter, subcluster speed estimates become increasingly inaccurate. The results for each method are summarised by relevant merger epoch in table 5.1.

During the first pre-pericenter epoch, 150 – 1400 Myr, we have moderately agreeing estimates ($\leqslant$ 35%) for both shock and DM halo, for density and temperature-based approaches. We can get a good agreement ($\leqslant$ 15%) between Rankine-Hugoniot derived estimates and the infaller-DM halo with the temperature-based average method. For first pericenter passage, temperature estimates agree well with infaller-DM halo speed. Temperature point also agrees well with shock speed ($\leqslant$ 10%), as well as temperature average though to a lesser extent ($\leqslant$ 20%). In the post-pericenter passage epoch, the strongest agreement measured overall takes place here, as either temperature-based estimate comes within $\sim$ 5% of the shock speed. Finally, with second pericenter passage, Rankine-Hugoniot estimates agree moderately with the measurements for both DM halo and the shock. Density-based estimates appear equally good for either subcluster or shock speed, during second pericenter passage and the first pre-pericenter epoch. With slightly better estimate agreement during second pericenter passage, inside 20% of the shock speed. Temperature average is equally as effective through 150 – 1600

		% Δ Infaller / Dark Matter Halo				% Δ Infaller / Shock			
Variable:		Temperature		Density		Temperature		Density	
Epoch (Myrs)	Data:	Point	Avg.	Point	Avg.	Point	Avg.	Point	Avg.
First Infall	Average	20%	6%	12%	9%	15%	13%	8%	10%
150 - 1400	Maxima	34%	13%	26%	21%	33%	31%	26%	26%
Pre-pericenter Passage	Std. Dev.	9%	4%	7%	7%	9%	9%	6%	7%
	Average	8%	6%	29%	32%	6%	9%	29%	36%
1400 - 1600	Maxima	14%	13%	48%	56%	10%	19%	52%	52%
Pericenter Passage	Std. Dev.	5%	4%	20%	25%	4%	8%	17%	14%
	Average	54%	55%	79%	109%	3%	2%	15%	33%
1600 - 2050	Maxima	114%	112%	146%	183%	4%	4%	30%	41%
Post-pericenter Passage	Std. Dev.	34%	34%	33%	39%	1%	1%	8%	7%
Second Infall	Average	27%	32%	10%	12%	17%	21%	9%	9%
4050 - 4250	Maxima	31%	55%	25%	25%	38%	59%	19%	19%
Pericenter Passage	Std. Dev.	5%	14%	8%	9%	14%	23%	7%	7%

Table 5.1: Percentage difference between Rankine-Hugoniot speed estimates and the DM halo or shock, per variable and data set, for relevant merger epochs. 'Pericenter Passage' encapsulates the period within ±100 Myrs of the pericenter passage, for both first and second infall. Remaining data is then divided between pre and post pericenter passage, note that for second infall there is only enough data to cover pericenter passage. Average and maxima values are highlighted according to their value, i.e., within 15%, green, between 15 – 35%, yellow, and outside 50%, red, relative to the DM halo and shock. Grey values lie between the yellow and red values 35 – 50%. Note that standard deviation is provided here to give indication of data spread around the average value.

Myrs, the first two epochs, where both the estimate average and maxima are in agreement within $\sim$ 5% and $\sim$ 15% of the DM halo, respectively. The temperature-based approaches, overall, provide moderate to good agreement for the shock through all epochs, and agree well with the DM halo except during first post-pericenter and second pericenter passage.

5.1.1 First Pre-pericenter Epoch

During the first pre-pericenter epoch, all methods track subcluster and shock speed moderately ($\leqslant$ 35%) to very well ($\leqslant$ 15%). Here, shock and subcluster speed are physically related as the infalling subcluster drives the shock. The density-based methods are consistent with one another, predicting either shock or DM halo speed within $\sim$ 25%. Temperature average provides the best speed estimate for the subcluster during this epoch, unlike temperature point which performs worst but still inside of 35% of the subcluster. Referring back to figure 4.4, between $\sim$ 600 – 1400 Myr, we see Rankine-Hugoniot jump conditions underestimate the subcluster speed but overestimate the shock speed, barring temperature point. The reason for the discrepancy between temperature-based but consistency between density-based approaches is clear from figure 3.2: temperature varies by over a factor of two in the shocked gas region, whereas density does not vary to the same degree. It is not obvious as to why temperature average provides the best result.

Regarding as to why the average Rankine-Hugoniot estimate underestimates the subcluster speed between 600 – 1600 Myr, during this phase the shock speed is slower than the subcluster speed, their discrepancy decreasing to $\sim$ 20%. In other words, while the bow shock is always ahead of the subcluster, the subcluster starts catching up with the shock. The distance between the shock and subcluster center decreases, the expected decrease in bow shock standoff distance, corresponding with increasing Mach number, is not the main reason for this disparity. Instead, the main contribution is likely ongoing ram pressure stripping, i.e., reduction of size of subcluster atmosphere. Thus, the upstream edge of the subcluster atmosphere moves slower than the subcluster's center due to the ongoing stripping. As it is the subcluster's upstream edge that drives the shock, the shock is slower as well. It would be interesting to verify this explanation by tracking the motion of the upstream edge through the

simulation.

5.1.2 First Pericenter Passage

Between 1400 – 1600 Myrs, first pericenter passage, temperature-based Rankine-Hugoniot estimates track the subcluster and shock speed both within almost $\sim 15\%$. The density-based estimates perform consistently worse, worsening still through pericenter passage, and should not be utilized. The reason for this apparent failure is due to host cluster's ICM density featuring the strongest radial gradient near the host cluster core. A small variation in chosen 'unshocked' gas location leads to a large change in unshocked density, resulting in a large uncertain in unshocked density. On the other hand, the temperature gradient in the host cluster ICM is much less steep, and subsequently less sensitive, resulting in better estimates. Investigating this sensitivity of the results to the positioning of data extraction regions would be useful.

5.1.3 First Post-pericenter Epoch

The greatest limitation when using Rankine-Hugoniot jump conditions to estimate the subcluster speed is the post-pericenter epoch of the merger. During the first post-pericenter epoch, Rankine-Hugoniot estimates cannot, and do not, trace the subcluster's infall speed as the shock is detached. We see this reflected in table 5.1, all estimates for the DM halo speed bear little resemblance to measurements taken between $1600-2050$ Myr. Here, the subcluster has passed the pericenter of its orbit, and whilst Rankine-Hugoniot jump conditions still estimate shock speed they do not estimate the subcluster speed any more. The reason is that after pericenter passage the subcluster does not drive the shock any more, i.e., the shock is no bow shock any more but a detached shock. The shock is no longer being driven by the infaller and is instead free to propagate forward under its own power. Additionally, the ICM's radial gradients means the shock does not necessarily lose energy as it propagates (Zhang et al., 2019a; Zhang et al., 2019b). We discussed earlier, section 5.1.1, that as long as the shock is driven by the infalling subcluster the shock and subcluster speed are physically related: we can assume that shock velocity $\approx$ infall velocity. The importance of pericenter passage

being that here this assumption breaks down. Post-pericenter, the infaller and individual gas elements are subject to greater deceleration than the shock itself. The consequence of this is a clear over-estimate of the subcluster's speed, as the subcluster decelerates and the shock does not.

Temperature-based Rankine-Hugoniot estimates track shock speed with excellent agreement, within $\sim 5\%$, whereas density-based estimates track only moderately well, about 35%. This is especially true of the density average method, which strongly over-estimates. The average for shocked density, like shown in figure 3.2, is based on the region between the shock position and the infaller upstream edge, i.e., the standoff distance. In the context of a runaway shock, this average increases over a not physically motivated larger and larger region. Furthermore, a strong underlying gradient present in the host cluster ICM density aggravates the problem. Even with the density-point method, the underlying ICM density gradient biases the shock speed estimate high near the host cluster core.

5.1.4 Second Pericenter Passage

When compared to first pericenter passage, temperature-based Rankine-Hugoniot estimates are less accurate during second pericenter passage. In figure 5.1, we can see sloshing and turbulence in the host cluster's ICM induced by the subcluster's first passage. Here, our temperature estimates are likely being impaired by this merger related random motion. Density-based estimates perform marginally better than during first pericenter passage, indicating density estimates are unaffected or, somehow, improved by these random fluctuations. We arrive at the interesting idea that, when the ICM ahead of the infalling subcluster better resembles the pristine, unperturbed, ICM of a relaxed galaxy cluster, we can use temperature-based estimates to retrieve a better approximation of infall velocity than might be afforded by a density-based estimate. When the host cluster has already been disturbed, e.g., due to a recent prior minor merger, density-based estimates are instead the better choice.

5.1.5 Estimating Unshocked Gas Conditions from the Simulation's Initial Conditions

As part of our investigation, we produced a set of estimates using the simulation's initial conditions for our unshocked gas values when using Rankine-Hugoniot jump conditions.

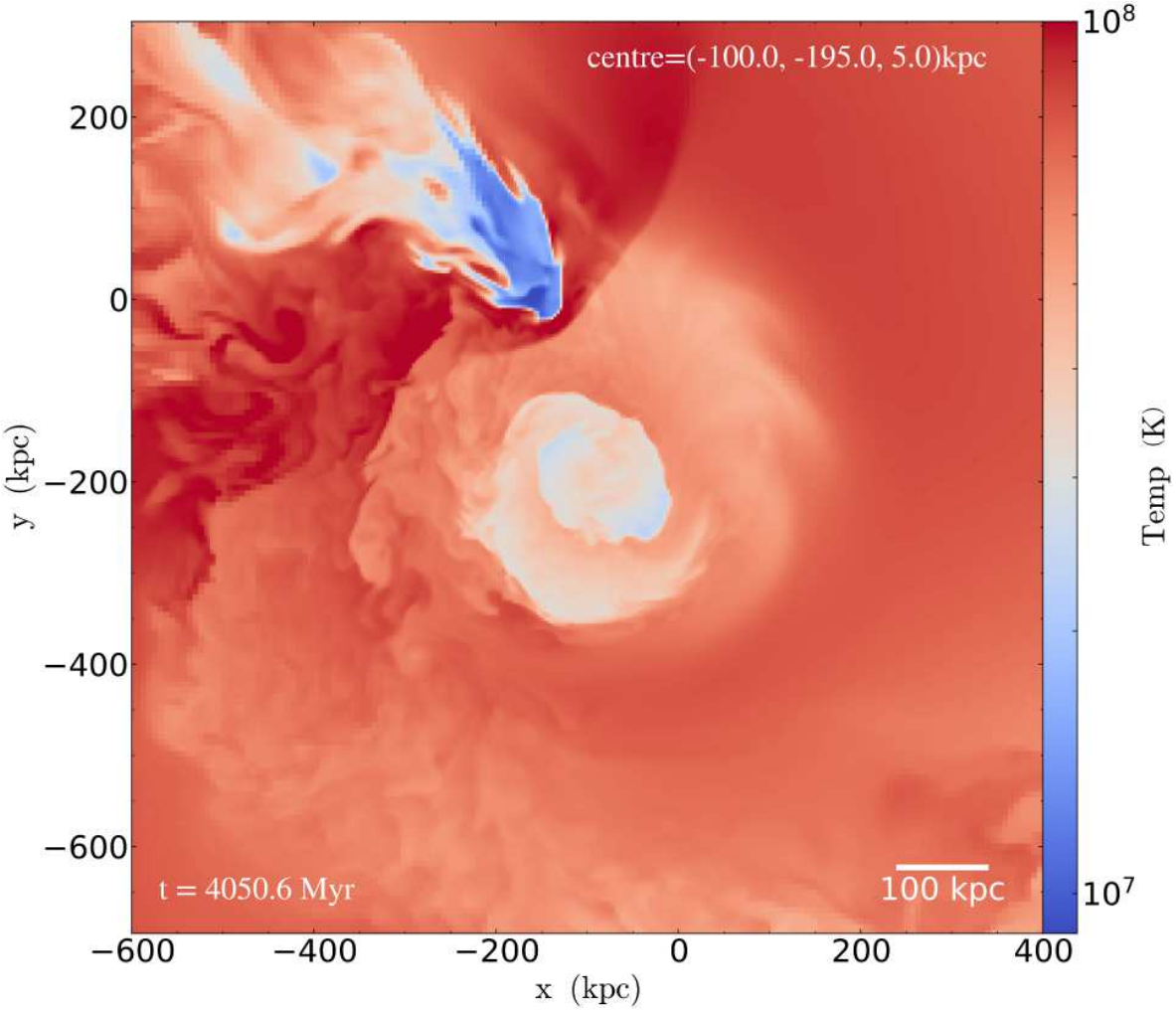

Figure 5.1: A temperature slice image showing our 1:10 minor merger during the second pericenter passage epoch (4050 Myrs). The slice is centered on the the host cluster, with the infalling subcluster north of its core position. Compared to the slice in figure 3.1, the host cluster ICM shows merger related substructure, e.g., sloshing cold fronts and turbulence-like random distortions.

Using the unshocked gas values, at the same radii relative to the host cluster, from the simulation's beginning, we use these values in lieu of the unshocked gas ahead of the infaller. Our analysis, however, indicates this approach did little to improve our estimates. Instead, using unshocked values from initial conditions produced results with more variance and more noise than those based on the current time step. We found that these approaches did little to change the overall scheme of things: Rankine-Hugoniot infall velocity estimates are fairly reliable until post-pericenter, at which they rapidly become unreliable. This indicates that care must be taken to extract the best possible unshocked gas conditions. As discussed above, especially the density is very sensitive to the locations of where the unshocked conditions are measure due to the strong ICM density gradients.

This is pertinent to both observers and theorists. In their work analysing a deep Chandra X-ray observation, and archival data, of a merger bow shock in A520, Wang et al. (2018) raise concerns regarding use of a wide sector to analyse bow shocks. They cite that a reduction in Mach number away from the 'nose' of the bow shock should be expected, as reported in Markevitch & Vikhlinin (2007), and that care should be taken using 'wide sectors' to analyse bow shocks, else the peak density jump will most likely be underestimated. Suggesting their estimated Mach number is reduced by $\sim$ 30% away from the shock's 'nose', where the shock front is oblique. Our results, and tests with 'initial conditions', reiterate this, that density measurements are extremely sensitive to change in position due to the ICM density gradient. As mentioned above, the temperature gradient throughout the cluster is not as steep, encompassing less than a magnitude, infall velocity estimates made using temperature as not as susceptible to positional error but still exhibit a wide range of results.

5.2 Applicability to Real Observations

5.2.1 Projection Effects

Our work has focused on simulations of galaxy cluster mergers, where we have direct access to all ICM properties in any location. In a real observation of a cluster merger, projections effects further complicate the analysis. This includes two complicating aspects.

First is when the line-of-sight to the galaxy cluster is not favourable, in such cases

we do not see the merger plane 'face-on'. The apparent bow shock and upstream edge of the subcluster are not the 'true' shock front and upstream edge. Here instead, the shock jump is weaker than precisely upstream, resulting in further underestimation. In their work, Machado & Lima Neto (2013) attempted to match the features of *A*3376 with N-body adiabatic hydrodynamical simulations using 'GADGET-2'. This merger is not directly in the plane of the sky, instead the angle between the 'collision axis' and the plane of the sky, or inclination, is 40°. Showing then how such an inclination would underestimate infall velocity if using Rankine-Hugoniot jump conditions, they report that this is a result of projection by contrasting against non-projected values. Density-made infall estimates are not immune to these effects, as Wang et al. (2018) report that care must be taken when analysing bow shocks, "...as the peak density jump will probably be underestimated". Suggesting that rapid Mach number falloff away from the cone ahead of the bow shock is to blame, with Mach values reduced by up to $\sim 30\%$. Given that viewing angles make regions of space appear larger, or smaller, it is feasible that measurements could be taken that are unintentionally underestimating. Needless to say, projection effects should be considered early before the use of Rankine-Hugoniot jump conditions to estimate infall velocity.

Secondly, the shocked and unshocked gas at the bow shock can only be seen through the cluster as a whole, with most of the gas along our line-of-sight being not of interest. This background contribution needs be either subtracted from observations, or modelled alongside the shock. Further increasing the uncertainty of shocked and unshocked density and temperature measurements, it is likely that the uncertainties we have deduced so far are lower limits.

ICM disturbance is also a factor acting to reduce the quality of measurements and subsequent velocity estimates. Given that galaxy clusters merge frequently, observers cannot make the assumption that the ICM is a pristine medium. We anticipate real-world cluster merger data might better resemble more conditions like the second infall in our simulations, rather than then any of the perfectly hydrostatic ICM during the first infall. Additionally, there is evidence to suggest that such disturbances are not short-lived. Sloshing cold fronts form when the host the cluster's central ICM is displaced from hydrostatic equilibrium inside

the cluster's gravitational potential. The ICM then oscillates, or sloshes, around hydrostatic equilibrium for many Gyr (e.g. Vaezzadeh et al., 2022).

According to the work presented here, density-based Rankine-Hugoniot velocity estimates seem less sensitive to such ICM disturbances and should be favoured. This result should be confirmed in a larger parameter study. Using wider sectors to measure the shocked and unshocked gas conditions could average out small-scale fluctuations. However, sectors too wide would suffer from the reduction of shock strength away from the apex of the bow shock (see also: Wang et al., 2018; Machado & Lima Neto, 2013). It could be possible to include this effect in a more detailed model in a future project.

6. Conclusion and Further Research

We found that Rankine-Hugoniot jump conditions are an effective predictor for the subcluster velocity, except when the subcluster moves away from the host cluster core. In the case of our simulated 1:10 minor merger, we were able to estimate subcluster velocity during pre-pericenter and pericenter passage. Regardless of infall phase, the 'average' Rankine-Hugoniot estimate of infall velocity was within 15%, at best, and 35%, at worst, of the subcluster velocity when made before post-pericenter passage. The reliability of the estimate varies depending on the variable and data used, temperature average infall velocity proved to be the best fit to the infaller's DM halo first infall, whereas density point method made for a better estimate during second infall. However, post-pericenter Rankine-Hugoniot jump conditions can track only the shock speed, with temperature-based better than density-based, but not the subcluster speed as the subcluster does not drive the shock anymore.

6.1 Future Work

Further investigation into the use of Rankine-Hugoniot jump conditions for estimating infall velocity, inside of simulation, is necessary to continue improving the confidence with which we can make such estimations. The following suggestions could be examined independently or in parallel.

This thesis used only one simulation. Repeating analysis for mergers of different mass ratios would give insights into how the accuracy of Rankine-Hugoniot speed estimates depends on the mass ratios. Whilst not investigated in our study, we suspect that more violent and energetic mergers, such as major mergers or those with further infalls, may result in estimates becoming more inaccurate.

In our approach, we measure shocked and unshocked ICM conditions in very small volumes, i.e., only along one forward ray. Increasing these volumes by adding additional rays, fanning out forward around the subcluster's direction of motion, would have several

advantages. This approach would help remove noise from the estimates, which would be most beneficial when assessing later infall periods, as well as better approximating how the method would be applied to real observations.

We note the sensitivity to positioning of data extraction regions as a point to investigate further. Density was particularly susceptible to this.

The largest step forward would be full modelling of the process used in observations to assess the impact of projection effects. Beginning with an optimal line of sight perpendicular to the plane of the merger, we suggest creating mock observations, images, and spectra. Then creating a simple analytic model of the undisturbed cluster with the embedded bow shock. This could be produced via a β-profile ICM with a simple ICM temperature profile, then predicting the images and spectra in important regions from the profile. Model parameters include: β-model parameters core radius, central density; temperature profile parameters; locations and size of the bow shock in the galaxy cluster; strength of the shock. These parameters need to be constrained by fitting the analytic model to the data. The result would be uncertainties in the shocked and unshocked density and temperature. Then, via Rankine-Hugoniot jump conditions, these translate to a final uncertainty in the infall speed estimate.

The findings of this thesis may also find some application in improving the velocity measurements of radio galaxy driven shocks, due to the close resemblance of Rankine-Hugoniot temperature based velocity measurements to shock measurements. Further evaluation in scenarios not involving galaxy cluster mergers may help verify the validity of such approximations.

Bibliography

Anderson J. D., 2011, Fundamentals of Aerodynamics, 5th edn. McGraw-Hill, New York

Ascasibar Y., Markevitch M., 2006, The Astrophysical Journal, 650, 102

Barrena R., Biviano A., Ramella M., Falco E. E., Seitz S., 2002, Astronomy and Astrophysics, 386, 816

Billig F. S., 1967, Journal of Spacecraft and Rockets, 4, 822

Cavaliere A., Fusco-Femiano R., 1976, Astronomy and Astrophysics, 49, 137

ESA XMM-Newton Digitized Sky Survey II Sanders J. S., 2020, X-ray and optical view of the Perseus galaxy cluster, https://www.esa.int/ESA_Multimedia/Images/2020/01/X-ray_and_optical_view_of_the_Perseus_galaxy_cluster

Emery D. L., Bogdán Á., Kraft R. P., Andrade-Santos F., Forman W. R., Hardcastle M. J., Jones C., 2017, The Astrophysical Journal, 834, 159

Fish T. M., 2020, PhD thesis, University of Hull

Forman W., et al., 2007, The Astrophysical Journal, 665, 1057

Fryxell B., et al., 2000, The Astrophysical Journal Supplement Series, 131, 273

Girardi M., Fadda D., Giuricin G., Mardirossian F., Mezzetti M., Biviano A., 1996, The Astrophysical Journal, 457, 61

Gould R. J., 1980, The Astrophysical Journal, 238, 1026

Hernquist L., 1990, The Astrophysical Journal, 356, 359

Irwin J. A., Sarazin C. L., 1996, The Astrophysical Journal, 471, 683

Keshet U., Markevitch M., Birnboim Y., Loeb A., 2010, Astrophysical Journal Letters, 719, L74

Kravtsov A. V., Borgani S., 2012, Annual Review of Astronomy and Astrophysics, 50, 353

Landau L. D., Lifshitz E. M., 1987, Fluid Mechanics. Pergamon Press, Oxford

Livio M., Regev O., Shaviv G., 1980, The Astrophysical Journal, 240, L83

Machado R. E., Lima Neto G. B., 2013, Monthly Notices of the Royal Astronomical Society, 430, 3249

Mahdavi A., Hoekstra H., Babul A., Balam D. D., Capak P. L., 2007, The Astrophysical Journal, 668, 806

Markevitch M., Vikhlinin A., 2007, Physics Reports, 443, 1

Markevitch M., Gonzalez A. H., David L., Vikhlinin A., Murray S., Forman W., Jones C., Tucker W., 2002, The Astrophysical Journal, 567, L27

Markevitch M., Govoni F., Brunetti G., Jerius D., 2005, The Astrophysical Journal, 627, 733

Mernier F., et al., 2018, Space Science Reviews, 214, 129

Mitchell R. J., Culhane J. L., Davison P. J. N., Ives J. C., 1976, Monthly Notices of the Royal Astronomical Society, 175, 29P

Mohr J. J., Mathiesen B., Evrard A. E., 1999, The Astrophysical Journal, 517, 627

Neumann D. M., et al., 2001, Astronomy and Astrophysics, 365

Nulsen P. E. J., Fabian A. C., 1980, Monthly Notices of the Royal Astronomical Society, 191, 887

Opher R., 1998, in 19th Texas Symposium on Relativistic Astrophysics and Cosmology. p. 533

Ostriker E. C., 1999, The Astrophysical Journal, 513, 252

Paterson A. R., 1983, A First Course in Fluid Dynamics. Cambridge University Press, Cambridge

Pratt G., Arnaud M., Biviano A., Eckert D., Ettori S., Nagai D., Okabe N., Reiprich T., 2019, Space Science Reviews, 215, 1

Roediger E., Lovisari L., Dupke R., Ghizzardi S., Brüggen M., Kraft R. P., Machacek M. E., 2012, Monthly Notices of the Royal Astronomical Society, 420, 3632

Roediger E., et al., 2015a, Astrophysical Journal, 806, 103

Roediger E., et al., 2015b, Astrophysical Journal, 806, 104

Roukema B. F., Quinn P. J., Peterson B. A., 1993, in Chincarini G. L., Iovino A., Maccacaro T., Maccagni D., eds, Astronomical Society of the Pacific Conference Series Vol. 51, Observational Cosmology. p. 298

Russell H. R., Sanders J. S., Fabian A. C., Baum S. A., Donahue M., Edge A. C., McNamara B. R., O'Dea C. P., 2010, Monthly Notices of the Royal Astronomical Society, 406, 1721

Schneider P., 2006, Extragalactic astronomy and cosmology: An introduction. Springer Berlin, Heidelberg

Schulreich M. M., Breitschwerdt D., 2011, Astronomy and Astrophysics, 531, A13

Sheardown A., et al., 2018, The Astrophysical Journal, 865, 118

Sheardown A., et al., 2019, The Astrophysical Journal, 874, 112

Simionescu A., et al., 2011, Science, 331, 1576

Sparke L. S., Gallagher J. S., 2007, Galaxies in the Universe: An Introduction. Cambridge University Press, Cambridge

Springel V., Farrar G. R., 2007, Monthly Notices of the Royal Astronomical Society, 380, 911

Su Y., et al., 2017, The Astrophysical Journal, 835, 19

Tanaka N., Furuzawa A., Miyoshi S. J., Tamura T., Takata T., 2010, Publications of the Astronomical Society of Japan, 62, 743

Tucker W., et al., 1998, The Astrophysical Journal, 496, L5

Turk M. J., Smith B. D., Oishi J. S., Skory S., Skillman S. W., Abel T., Norman M. L., 2011, The Astrophysical Journal Supplement Series, 192, 9

Vaezzadeh I., et al., 2022, Monthly Notices of the Royal Astronomical Society, 514, 518

Van Dyke M., 1982, An Album of Fluid Motion. Parabolic press, Standford

Vikhlinin A., Markevitch M., Murray S. S., 2001, The Astrophysical Journal, 549, L47

Vitvitska M., Klypin A. A., Kravtsov A. V., Wechsler R. H., Primack J. R., Bullock J. S., 2002, The Astrophysical Journal, 581, 799

Wang Q. H. S., Markevitch M., Giacintucci S., 2016, The Astrophysical Journal, 833, 99

Wang Q. H. S., Giacintucci S., Markevitch M., 2018, The Astrophysical Journal, 856, 162

Wechsler R. H., Tinker J. L., 2018, Annual Review of Astronomy and Astrophysics, 56, 435

White S. D. M., 1976, Monthly Notices of the Royal Astronomical Society, 174, 19

Zhang C., Yu Q., Lu Y., 2016, The Astrophysical Journal, 820, 85

Zhang C., Churazov E., Forman W. R., Jones C., 2019a, Monthly Notices of the Royal Astronomical Society, 482, 20

Zhang C., Churazov E., Forman W. R., Lyskova N., 2019b, Monthly Notices of the Royal Astronomical Society, 488, 5259

Zhang C., Churazov E., Zhuravleva I., 2021, Monthly Notices of the Royal Astronomical Society, 501, 1038

Zhuravleva I., et al., 2014, Nature, 515, 85

ZuHone J. A., 2011, The Astrophysical Journal, 728, 54

ZuHone J. A., Roediger E., 2016, Journal of Plasma Physics, 82, 48

ZuHone J., Markevitch M., Johnson R., 2010, The Astrophysical Journal, 717, 908